Filip Feldesi

Three-Dimensional Contact Patch Strain Measurement Inside Rolling Off-Road Tyres

University of Pretoria

Supervisors: Dr T.R Botha and Prof. P.S Els

Submitted in partial fulfilment of the requirements for the degree

Master of Engineering (Mechanical engineering)

In the faculty of

Engineering, Built Environment and Information Technology

At the

University of Pretoria

October 2018

Abstract

The forces generated in the tyre contact-patch are important for vehicle dynamics analysis. The tyre contact patch is not directly visible due to the terrain. Measuring the strain in the contact patch region may give insight into the forces generated by the tyre as it deforms. Strain measurement in the contact patch is often limited to discrete points, using strain gauges or other techniques which limits data capture to once per revolution. In this study stereovision cameras are used to capture unique features in the pattern painted on the tyres inner surface. An in-tyre mechanically stabilized camera system allows the contact patch to be captured continuously and the stereovision cameras allow for full field measurement of the tyre inner surface. In post processing the features are tracked and triangulated to form point-clouds for each time step. Point-clouds are compared to determine the strain of common points in two directions. The system is applied to an agricultural tyre with large tread-blocks. The wheel is instrumented to measure pressure and forces. The tyre is tested statically in a series of tyre tests where the lateral, longitudinal and vertical displacement is controlled. The strain measured in the tyre contact patch region is compared to the forces measured at the wheel centre. It is noticed that as the measured forces increases so too does the magnitudes of the strains. Unique patterns are found in the contact patch strain for each test type. These patterns could be used to identify the type of forces experienced by the wheel while the strain magnitude could give an indication of the magnitude of the forces. Future work could allow for strain measurement in the contact patch as the tyre rolls over deformable terrain where displacement is not easily controlled.

Keywords: stereovision, point-clouds, large tread-blocks, contact-patch strain.

Acknowledgements

I would like to express my special thanks of gratitude to Dr TR Botha for assisting me in this project. His extensive knowledge in the field of stereovision and its unique application in vehicle dynamics guided me in the right direction.

I would like to express my special thanks of gratitude to Prof PS Els for assisting me in this project. His mentorship guided me when I encountered problems and his knowledge helped in areas which I am not too familiar with.

Contents

List of Figures

List of Tables

List of Symbols

Symbol	Description	Units
A	Subset of depth resolution function	
AT	Area of triangle	mm^2
B	Subset of depth resolution function	
c	Circle of confusion	mm
$\frac{dv}{dy}$	Vertical displacement gradient in y-axis	
$\frac{du}{dx}$	Horizontal displacement gradient in x-axis	
$\frac{du}{dy}$	Horizontal displacement gradient in y-axis	
$\frac{dv}{dx}$	Vertical displacement gradient in x-axis	
e_l	Left epipole	
e_r	Right epipole	
f	Focal length	mm/pixel
$f(\mathrm{x},\mathrm{y})$	Grayscale of reference image at pixel coordinates (x, y)	
f_m	Average grayscale value of subset in reference image	
G	Gain	dB
$g(\mathrm{x},\mathrm{y})$	Grayscale of current image at pixel coordinates (x, y)	
g_m	Average grayscale value of subset in current image	
K	Stiffness	N/mm
N	Aperture	f-stops
N_{pn}	Number of teeth on planet gear n	
N_{sn}	Number of teeth on sun gear n	
O_l	Projection centre of left camera	
O_r	Projection centre of right camera	
P	Power	Watt
P_n	Point in three-dimensional space	
P_l	Projection of point P on the left image plane	
P_r	Projection of point P on the right image plane	
Ps	Pressure	Bar
R^2	Coefficient of determination	
s	Distance to surface	mm
t	Baseline	mm
u	Horizontal displacement component	Pixels
u_n	Longitudinal deformation of the n node	mm
v	Vertical displacement component	Pixels
V	Volts	V
v_n	Lateral deformation of the n node	mm
vs	Vehicle speed	km/h
x	Camera image plane coordinate x	mm
X	Global coordinate x	mm
$x_{cur_{ij}}$	Current image x-coordinate of subset particle i, j	Pixel
x_{nm}	Difference between the x coordinate at n and m	mm
x_{Pl}	X coordinate of point P in the left image plane	mm

Symbol	Description	Units
x_{Pr}	X coordinate of point P in the right image plane	mm
x_{ref_c}	Subset x-centre of reference image	Pixel
$x_{ref_{ij}}$	Reference image x-coordinate of subset particle i, j	Pixel
y	Camera image plane coordinate y	mm
Y	Global coordinate y	mm
$y_{cur_{ij}}$	Current image y-coordinate of subset particle i, j	Pixel
y_{nm}	Difference between the y coordinate at n and m	mm
y_{Pl}	Y coordinate of point P in the left image plane	mm
y_{Pr}	Y coordinate of point P in the right image plane	mm
y_{ref_c}	Subset y-centre of reference image	Pixel
$y_{ref_{ij}}$	Reference image y-coordinate of subset particle i, j	Pixel
Z	Distance to point	mm
Δd	Minimum measureable disparity	mm
ΔZ	Depth resolution	mm
B	Subset of depth resolution function	
γ_{xy}	Shear strain	
ε_x	Longitudinal strain	
ε_y	Lateral strain	
φ	Pan angle	Rad
ω_c	Rotational speed of carrier ring	Rad/s
ω_{pn}	Rotational speed of planet gear n	Rad/s
ω_{sn}	Rotational speed of sun gear n	Rad/s

Abbreviations

CAD	Computer Aided Design
CST	Constant Strain Triangle
CTPE	Conductive Thermoplastic Elastomers
DAQ	Data Acquisitioning System
DIC	Digital Image Correlation
DOF	Depth of Field
IC-GN	Inverse Compositional Gauss-Newton
LED	Light Emitting Diode
MOSFET	Metal-Oxide-Semiconductor Field-Effective Transistor
SAD	Sum of Absolute Difference
SLSQP	Sequential Least Squares Programming
T2Cam	Tyre Terrain Camera
WFT	Wheel Force Transducer
ZNSSD	Zero-mean Normalized Sum of Squared Difference

Introduction

Apart from aerodynamic forces, all the forces acting on the vehicle are generated in the tyre contact patch. When considering the tyre characteristics in vehicle dynamics, empirical data is often used in simulations. The empirical data is obtained through repeated tyre tests on a homogeneous surface through a wide range of operating conditions. In terramachanics, the terrain is constantly changing and therefore empirical data cannot be established using conventional tests. It is necessary to understand how the forces are generated over the entire contact patch region by analysing how the contact patch deforms. This study demonstrates how the contact patch strain can be measured and possibly related to the overall forces generated by the tyre.

Full field measurement of the contact patch is challenging due to the rotational nature of the inflated tyre. The tyre is exposed to harsh environments such as dirt and rain and experiences large forces and deformations. Measurements in the contact patch region must not affect the performance or operating conditions of the tyre. The area of the tyre in contact with the terrain is only visible from the inside of the tyre as the outside is obscured by the terrain. Thus, the best approach to measure the region in contact with the terrain is from the inside. A mechanically stabilised system inside the tyre is chosen with an optical measuring system to not affect the tyre performance.

This study begins with and overview of relevant literature (Chapter 1). The tyre contact patch is discussed and different approaches to measuring strain in the tyre are analysed. The suitability of a mechanically stabilised stereovision measuring system is explained in Chapter 2. An overview of stereovision and its application is given. Accuracy and processing speed are important considerations when setting up a stereovision system. Differences between two digital image correlation algorithms are discussed. The details of the stereovision system and the experimental work are presented. Camera position, lighting and digital image correlation

are addressed, and experimental tests are presented. Overall strain measurement and accuracy are discussed.

With the stereovision system setup, the system is implemented on an agricultural tyre with large tread-blocks in Chapter 3. The effect of large tread-blocks on the variations of strain in the tyre is investigated. The tyre is tested on a static tyre test rig where the lateral, longitudinal and vertical displacements can be controlled. Various tests are performed measuring the forces at the wheel hub centre and using the stereovision system to measure the strain in the contact patch region. The forces and strains are compared. Unique patterns are found in the contact patch for each type of loading case. The patterns reveal suitable regions for a single-point strain measurement. The single-point value, analogous to a strain gauge on the inner surface, is compared to the measured forces. Full field strain measurement is necessary to understand the contact patch region under different loading conditions but in future could be replaced with a few single point measurements in the tyre with the purpose of developing a smart tyre.

1) Literature Review

According to Gillespie (1992) the tyre serves three basic functions namely:

- It supports vertical load and cushions road shocks.
- It develops longitudinal forces for accelerating and braking.
- It develops lateral forces for cornering.

Tyres have complex construction consisting of rubber and steel or fabric plies in different layers and different directions. Tyre modelling is complex and due to the large construction varieties cannot be generalised. An example of a radial tyre is shown in Figure 1 which indicates the basic structure of a tyre.

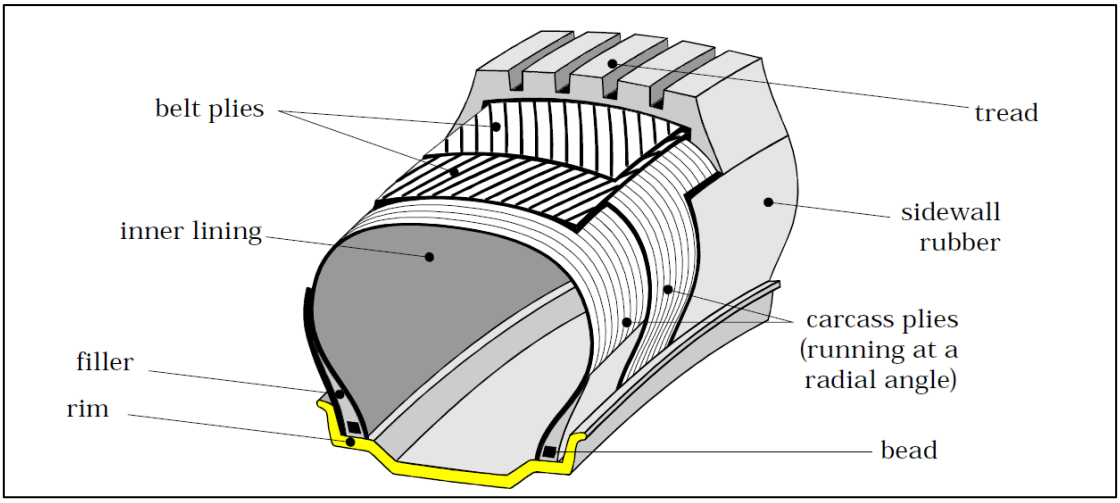

Figure 1- Tyre Construction (Zegelaar, 1998)

1.1) Tyre contact patch strain

The tyre contact patch is the portion of the tyre that is in contact with the road or terrain. Apart from aerodynamic forces all the forces on a vehicle are generated in the tyre contact patch (Gillespie, 1992). Many approaches to measuring the contact patch have been attempted by researchers and examples of each will be discussed. The approaches are grouped based on the region of the tyre that the method focused on. The advantages and disadvantages of each type of approach is also discussed.

1.1.1) Analysis of tyre contact patch from below

While the contact patch is not directly visible, the tyre can be pressed on a glass plate while pictures of the contact patch are taken using a camera below the glass as can be seen in Figure 2. This method, as presented by Ivanov (2010), is useful for analysing tyres during static type tests.

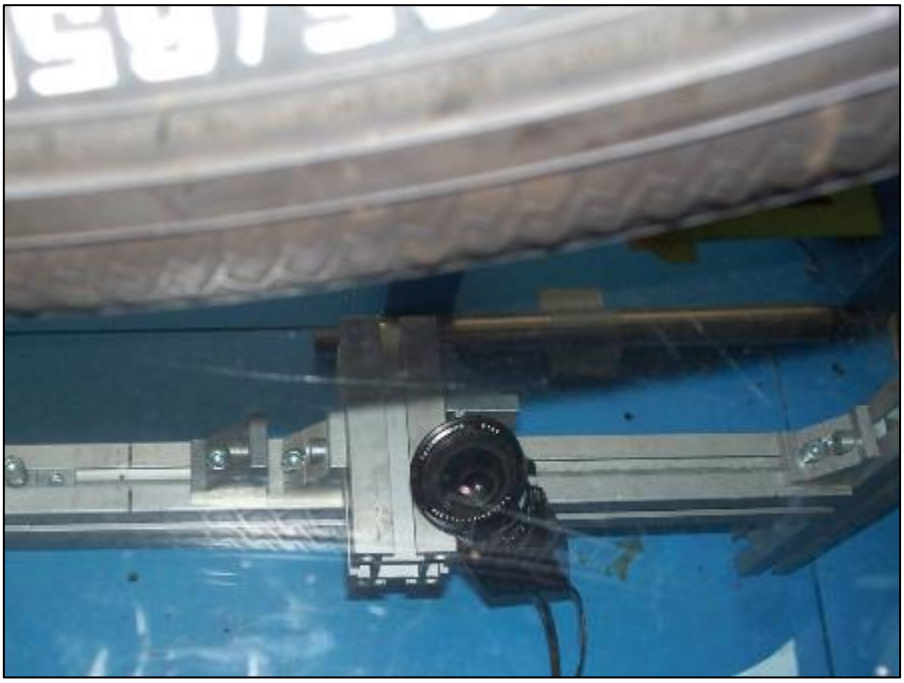

Figure 2- Tyre contact patch test rig (Ivanov, 2010)

This type of setup is relatively simple and does not require any modification to the tyre or wheel. Ivanov uses this method to allow for easy relative comparison of different tyres using a few simple static tests. The method uses visual processing to track points in the contact patch as the glass plate is slowly moved underneath the tyre. While Ivanov limits the work to relative comparison of contact patches, Ivanov concludes that analysis of the contact patch would be possible in future works using similar methods. Tracking a full field of points could allow for strain measurement in the contact patch region using optical methods. There is a risk of glass distortion which would affect the accuracy of the optical measurements. This setup is limited to analysing tyre contact patches on flat and smooth glass surfaces. Since the glass is smooth

only small strains can be produced therefore the glass is not fully representative of road conditions and therefore only relative performance of tyres can be obtained. The method cannot be used in the terramechanics application where the tyre terrain interaction is desired.

1.1.2) Contact patch forces measured through road surface

Measuring the contact stresses in the road can be directly related to the stresses in the contact patch. By creating a road surface pad that can measure stresses, through force transducers, the contact patch can be analysed over more realistic road surfaces. An array of sensing elements, as shown in Figure 3, allows for full field stress measurements of the contact patch as the tyre rolls over the pad. The compact form factor allows for the pad to be placed on the road to analyse the contact patch in-situ dynamic tests as demonstrated by Anghelache and Moisescu (2012). Using force transducers allows for measurement of forces in all three directions. The system has limitations in resolution as the system only has a finite number of transducers, 30 sensing elements, arranged in the lateral direction. The 30 elements result in a lateral resolution of 10mm. A higher resolution is achievable in the longitudinal direction but tracking the position of the wheel on the pad is crucial. Anghelache and Moisescu (2012) use an optical transducer connected to a mobile data aquisitioning device to track the longitudinal speed and displacement and a camera to allow the driver to align the vehicle in the lateral direction. Tests are limited to straight line tests because only a small section of the road is instrumented therefore a long distance is needed to align the tyre and pad. The pad is adequate for driving, free-rolling and braking tyres at diffrenet speed ranges. Pottinger (2006) highlights the importance of mounting the transcduces flush with the road surface and the gap around the transducer. The gap around the tranducers is necessary to ensure that there is no force grounding and force passes through the transducer. These considerations make measurements tedious as the surface and tyre need to be checked for debris that might affect the measurements. The

system is not ideal for terramechanics as the pad needs to be embedded into a deformable soil. The soil covering the pad can affect the accuracy and results of the measurement.

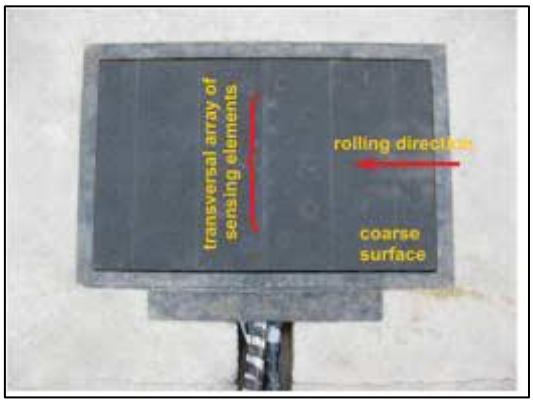

Figure 3- Road Surface Pad to Measure Contact Patch Stresses (Anghelache and Moisescu, 2012)

1.1.3) Tyre strain inside the tyre construction

Tyres experience large deformations and strains. This makes strain measurement in the tyre construction rather complex. The sidewalls may have a different stiffness compared to the tread. The tread may also have very different stiffness in the longitudinal and lateral directions. Garcia-Pozuelo, et al (2019) uses Kyowa strain gauges (KFEL-2-120-D35L1M2S) on the tyre inside surface to measure strain in a small slick tyre for SAE Formula Student. The large-strain strain gauge can measure from -5000 to 5000 microstrain. The circumferential strain measured in the tyre on a rolling drum, at 10km/h and 750N vertical load, is shown in Figure 4.

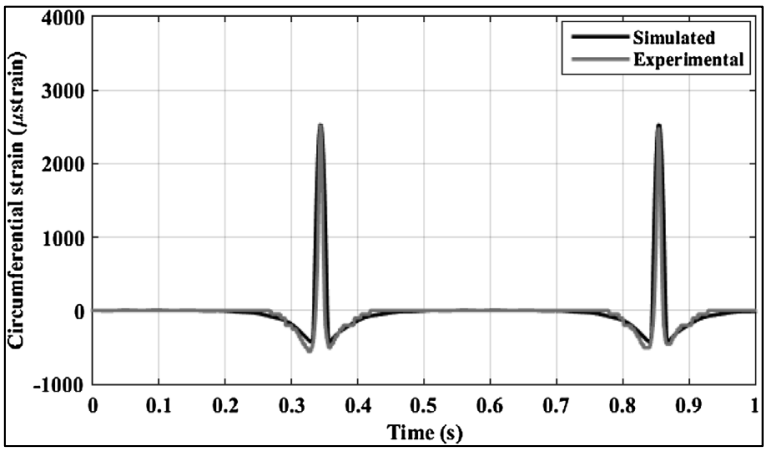

Figure 4- Circumferential Strain Measured on Rolling Drum at 10km/h (Garcia-Pozuelo, et al., 2019)

In a small relatively stiff tyres this range is suitable. Agricultural tyres are expected to have larger strains and therefore typical strain gauges are not suitable. Advances in sensors have allowed for high strain measurement. Ruggeri and Vecchiattini (2018) developed a conductive thermoplastic elastomers (CTPE) sensor to measure strain in the contact patch region as seen in Figure 5. The sensor has a similar stiffness to the tyre and therefore does not affect the tyre behaviour or performance. Three sensors measure strain in three directions over three select lines, measuring the average strain, but can be adapted to produce measurements over many locations to potentially produce full field measurements. The geometry of the sensor and material can be varied to suit the application. Ruggeri and Vecchiattini (2018) use the longitudinal sensor to measure longitudinal strain in a tyre as it is rolled over a flat surface and as it is rolled onto a small step, seen in Figure 6. While Ruggeri and Vecchiattini (2018) have managed to measure strains in the contact patch region, the sensors are in the early stages of testing and would need to be tested for repeatability and sensitivity to operating conditions.

Figure 5- CTPE Prototype Strain Sensor Showing One Sensor (Ruggeri and Vecchiattini, 2018)

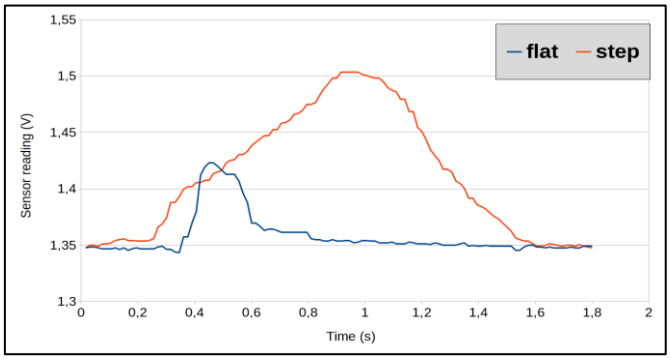

Figure 6- Longitudinal CTPE Strain Measurement in Tyre (Ruggeri and Vecchiattini 2018)

Matsuzaki and Akira (2006) proposed using the existing steel chords in the tyre to measure strain as seen in Figure 7. The method could provide full field strain measurements using the tyre as a sensor itself thus not affecting the performance and behaviour of the tyre. Tests were only performed on small sections of tyre and would be difficult to implement on a full tyre. A full tyre implementation would require a custom manufactured tyre and data acquisition system with many uncertainties on precision and sensitivities. The system would also be limited to one specific tyre so relative comparisons would not be possible. Placing single point strain sensors inside the tyre can be used to create smart tyres. The question of how many and where to place the strain sensors especially for agricultural tyres with large tread-blocks becomes an important question.

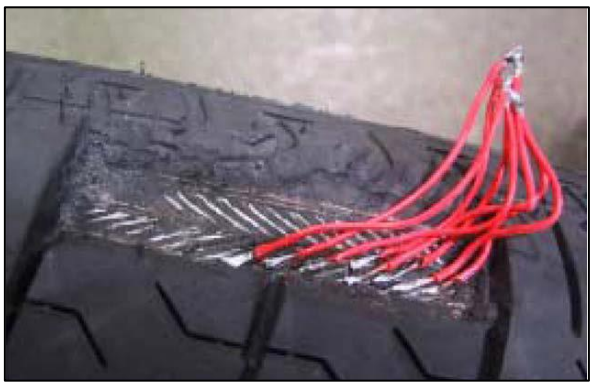

Figure 7- Strain Measurement using Steel Tyre Chords (Matsuzaki and Akira, 2006)

1.1.4) Contact patch measured from the inside of the tyre

Non-contact systems can capture the tyre surface in the region where road contact occurs without affecting the performance or behaviour of the tyre. Xiong and Tuononen (2014) mounted a laser and sensor to the inside of the rim to measure the deformation of one point in the tyre inner surface as it rotates into and out of the contact patch. This system can accurately measure the displacement of the tyre at the location of the laser but does not measure the displacement of a specific point on the tyre. To measure the strain on the tyre surface, the position of at least two points on the tyre need to be known. As the tyre deforms the change in

position of the points can be used to numerically determine the strain. Hiroaka, et al (2009) first proposed using a single camera inside a pneumatic tyre mounted to the wheel rim pointing at the contact patch. The camera uses Digital Image Correlation (DIC) to track unique points in a pattern on the inner surface of the tyre. The system could measure in-plane strain in the contact patch region. The system also used spotlight projection in the form of a set of lasers which are recorded by the camera to determine the out of plane displacement. The out of plane displacement is used as a correction for the plane strain to compensate for apparent strain caused by objects appearing bigger when they move closer to the camera.

Matsuzaki, et al (2010) later adapted the system to measure out of plane displacement without the use of spotlight projection. Rubber blocks glued to the inner surface allow for three dimensional measurements using the out of plane surface on the top of the rubber block. The system uses DIC techniques to measure an apparent strain on the base (tyre surface) and top surface (block surface). Matsuzaki, et al (2010) determines a relationship between the top base surface strain and then uses the relationship to determine the out of plane displacement. The system uses a discontinuos surface which makes DIC difficult and computationally expensive. The system does involve sticking large rubber blocks on the inner surface of the tyre which may affect the behaviour and performance of the tyre and is thus not suitable for dynamic testing.

Green (2011) attempted to obtain high-resolution full-field deformation using the single camera method like Matsuzaki, et al (2010). Green achieved high-resolution image correlation with fine sub-pixel interpolation using bi-cubic spline interpolation allowing for a continuous representation of the intensity surface while relying only on intensities at integer locations. Green was unable to determine the out of plane effects on strain with a novel technique based on image blur to extract depth. Green uses the system on a passenger car tyre which deflected in the vertical direction as seen in Figure 8 at 2mm increments. The machine pushes the tyre

onto a plate from the top of the tyre. This results in deflections of the tyre on both sides of the wheel hub.

Figure 8- Deflecting Tyre in Vertical Direction (Green, 2011)

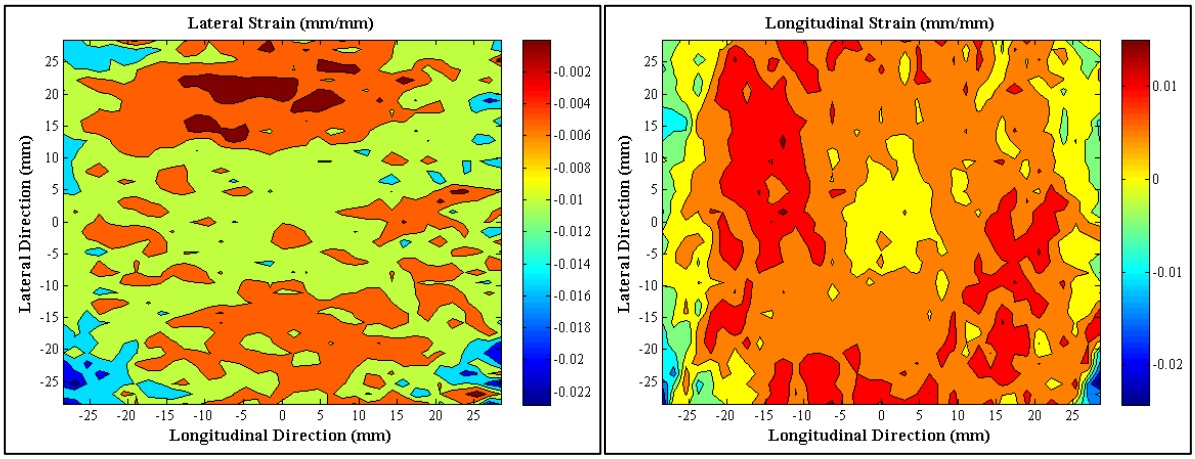

Figure 9- Lateral and Longitudinal Strain for 10mm Deflection (Green, 2011)

Lateral and longitudinal strain measured by the system, for 10mm deflection, are shown in Figure 9. The single viewpoint used meant that Green was not able to account for out of plane effects which cause apparent strain. Green finds an increase in longitudinal strain with an increase in vertical deflection but notes that lateral strain is mostly negligible. The work by Green suggests that while the tyre contact patch is mostly planar a high depth resolution, for out of plane effects, is necessary to achieve quantitative results. Green measures the strain in a

line through the centre of the contact patch in the longitudinal direction for longitudinal strain distribution and in the lateral direction for lateral strain distribution. The measured longitudinal strain and lateral strain is shown in Figure 10 and Figure 11 respectively. The longitudinal strain shows an increase in front and behind the centre at the contact patch region however this could be due to apparent strain caused by out of plane displacement.

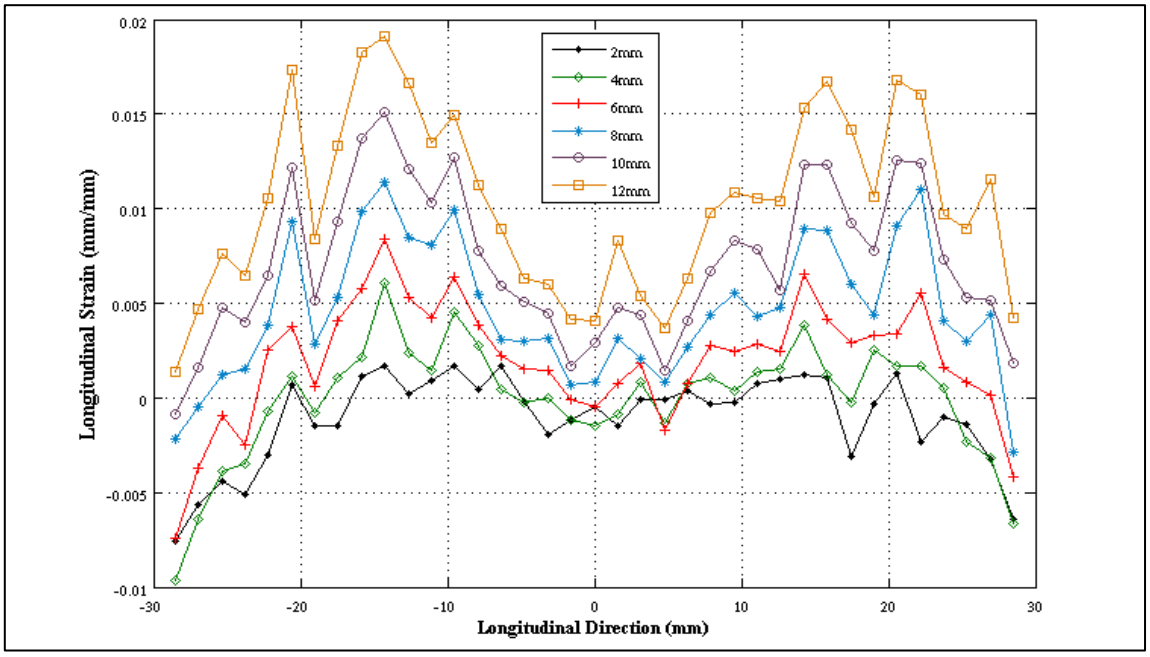

Figure 10- Longitudinal Strain Profile at Longitudinal Centre Line (Green, 2011)

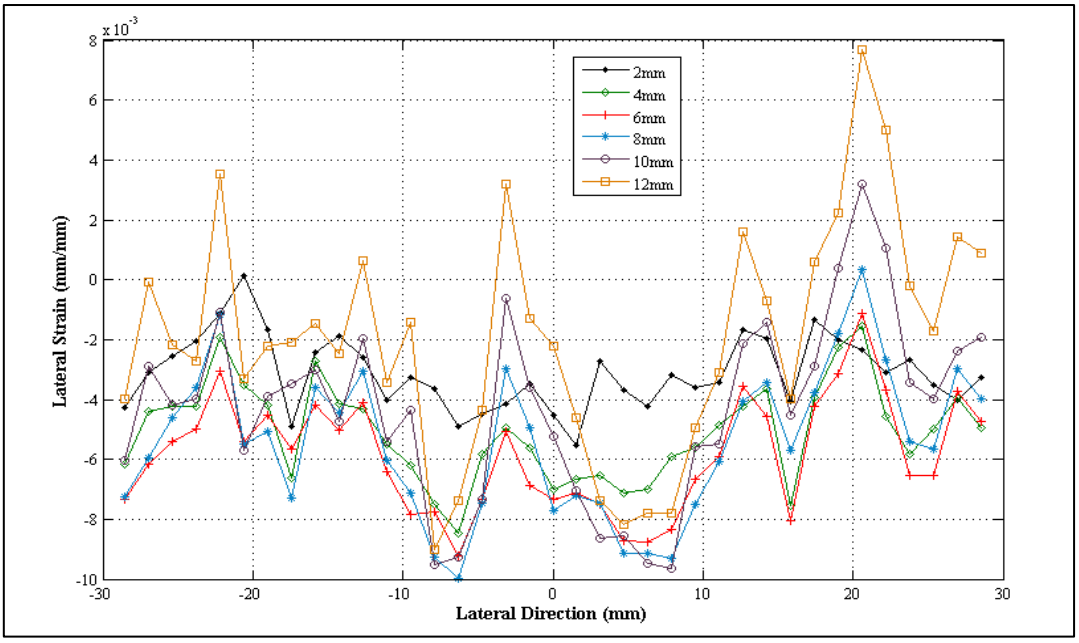

Figure 11- Lateral Strain Profile at Lateral Centre Line (Green, 2011)

Green (2011) measures less than 2% strain in the longitudinal direction and less than 1% strain in the lateral direction. Green was not able to account for out of plane and apparent strain and therefore no conclusions can be drawn on the strain distribution. Small strain amounts are difficult to analyse and to draw clear conclusions due to the presence of noise.

Guthrie, et al (2017) used two cameras in a stereo configuration to determine the full field deformation of the inside of the tyre at the contact patch region. The system makes use of a mechanically stabilised system inside the wheel to which the two cameras and an embedded computer are mounted. The system is mounted on a vehicle to measure deformation during a dynamic test. The inner surface can capture deformations, caused by an object, in the contact patch as seen in Figure 12, where the tyre is driven over a 50mm square cleat. Figure 13 shows a longitudinal cross-section of the contact patch during the same test.

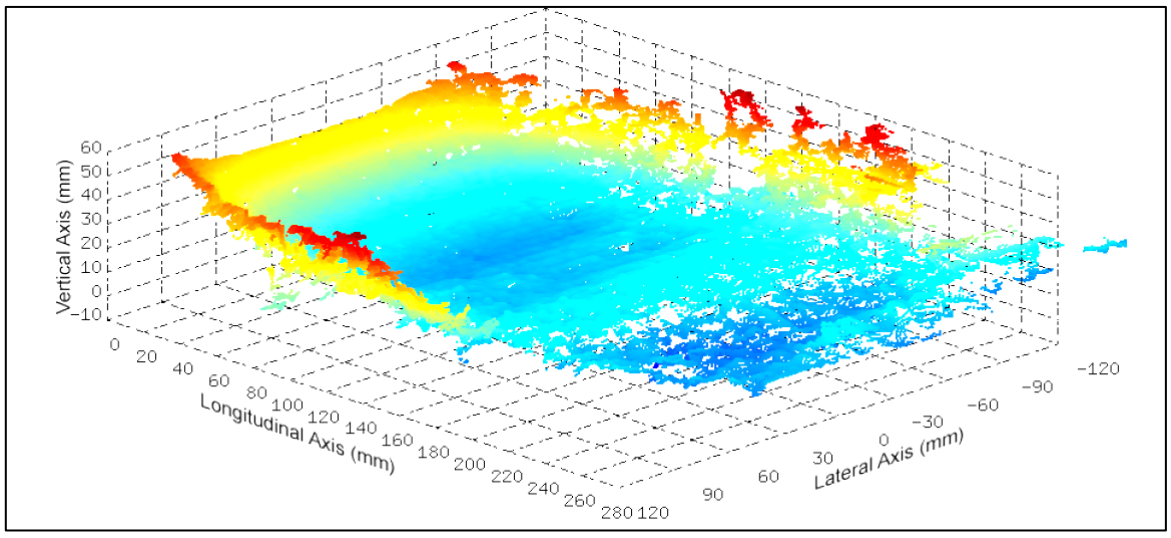

Figure 12- Inner Surface of Tyre Contact Patch during Cleat Test (Guthrie, 2016)

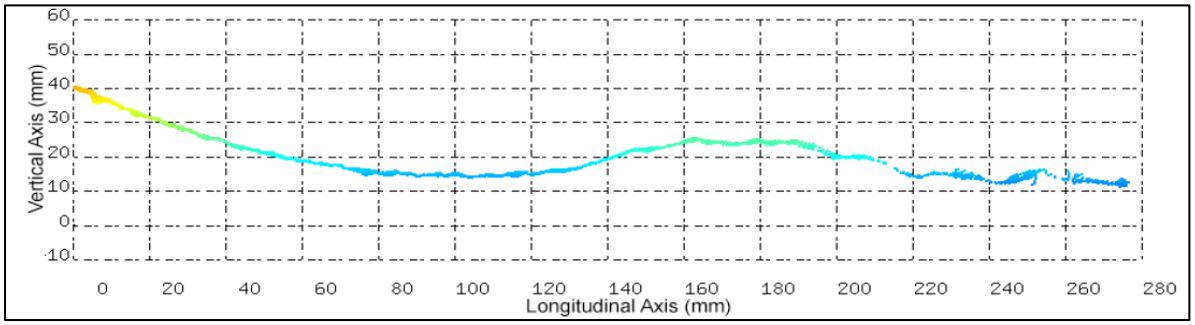

Figure 13- Longitudinal Section Through Tyre Contact Patch during Cleat Test (Guthrie, 2016)

The system can capture full-field three-dimensional deformation in the tyre, but the results are noisy and there are many lost points. The two cameras are mounted side by side behind the contact patch facing forward and as a result the resolution of the points decreases further away from the cameras and resulting in lost points further from the camera. Guthrie, et al (2017) recognizes the possibility of using the system to optically determine the strain on the inside of the tyre in the region where the tyre contacts the terrain. The three-dimensional location of points could be used to determine the out of plane effects on measured strain.

The systems presented each have considerable merit when considering strain measurement in the contact patch. However, none of the systems in their current form provide a robust method for measuring contact patch strain for a variety of tyre tests especially in terramechanics situations. The methods that analyse the contact patch from below are only able to capture the tyre at one point in the road limiting the potential strain measurement to static type tests or very limited dynamic tests. These measurements may also be sensitive to debris or distortion of the glass plate. Methods that measure strain in the tyre structure are difficult to implement and would require further development to achieve a full field sensing system but would have the advantage of being insensitive to debris and should allow a variety of tyre tests. Methods that measure the contact patch from inside the tyre have the advantage of being sealed from external debris and do not affect the performance of the tyre. The system presented by Guthrie, et al (2017) is not able to measure strain but can be adapted. The system is suitable for dynamic tests even over rough terrain and is available for this study. It is used as the basis for this study and is presented in more detail.

1.2) In tyre stabilization

Guthrie, et al (2017) developed a mechanical system for stabilization of the cameras inside the tyres namely T2Cam (Tyre Terrain Camera) shown in Figure 14. The stabilisation system allows the cameras to be pointed at the contact patch while the tyre is rotating during dynamic

tests. The system makes used of two sets of planetary gears. The cameras are mounted to a sun gear on the inside of the inflated tyre. A planet gear meshes with the sun gear and is connected to a shaft that leads to the outside of the wheel. On the outside a second planet gear and sun gear are used. The number of sun gear teeth inside and outside are equal, and the number of planet teeth inside and outside are equal, therefore the speed of the inside and outside planet gears is equal. When the gear on the outside is held stationary the sun gear on the inside remains stationary while the planet gears and wheel rotate. Once the system is sealed it can only be accessed wirelessly to transfer images captured by the cameras. The system is powered by 12V brushes that connect to a 12V battery on the outside of the wheel.

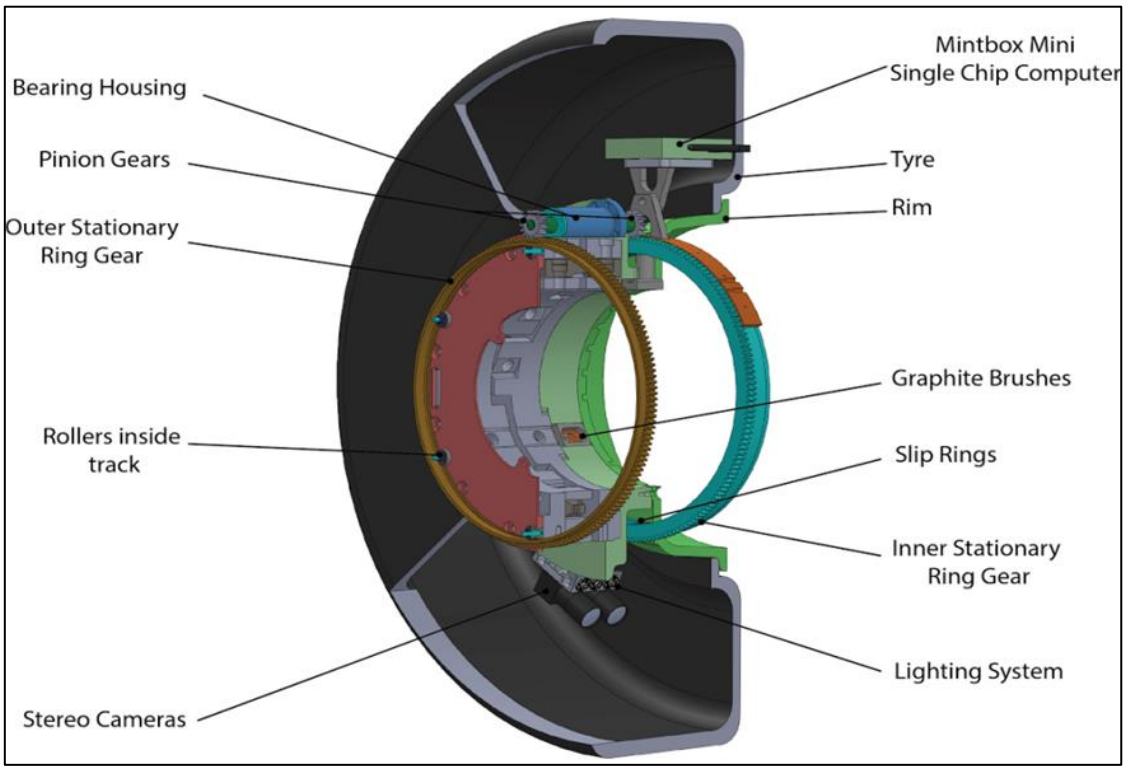

Figure 14- Mechanical Stabilisation for Rotating Wheel (Guthrie, et al., 2017)

1.3) Stereovision

Digital cameras focus light through a lens onto an image sensor. The image sensor is comprised of discrete photodiodes arranged in a two-dimensional matrix which record the light intensity when exposed to light. Prince (2012) presents a pinhole camera model which is a simplification of a real camera but can be used to easily relate real world coordinates to image

plane coordinates. In this model all light rays converge to a single focal point (pinhole) and are projected onto an image plane. The pinhole camera model in the x (horizontal) direction is shown in Figure 15.

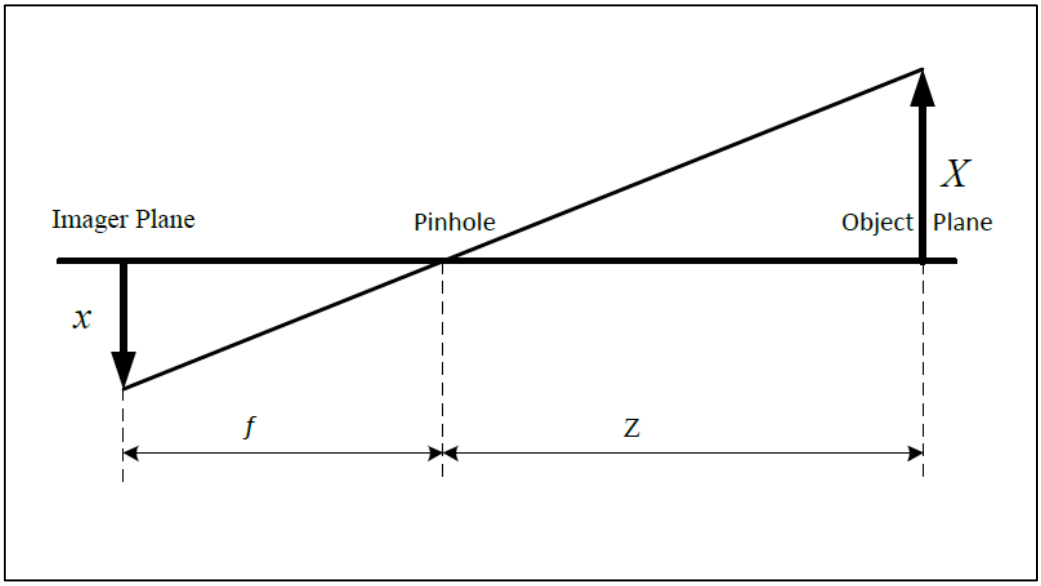

Figure 15- Pinhole Camera Model (Botha, 2015)

The horizontal coordinate of the point on the image plane is x and the position of the point in the real world is X. The distance from the pinhole to the object plane is Z while the distance to the image plane is f, also known as the focal length. Equation 1 is used to relate image plane coordinates to real world coordinates.

$$x = f\frac{X}{Z} \tag{1}$$

The same is true for the relating the y (vertical) coordinate on the image plane to a real-world Y (vertical) coordinate and Equation 2 is used.

$$y = f\frac{Y}{Z} \tag{2}$$

Stereovision involves using two cameras to extract the three-dimensional information of a scene. In Figure 16, these cameras are illustrated as an image plane and a theoretical focal point where all light rays converge. An arbitrary point P is projected on both image planes as

P_l and P_r. The point O_l and O_r is the focal point of the left and right camera respectively. Using the relative position of the two camera focal points, triangulation is used to determine the three-dimensional position of the point P relative to the cameras focal point.

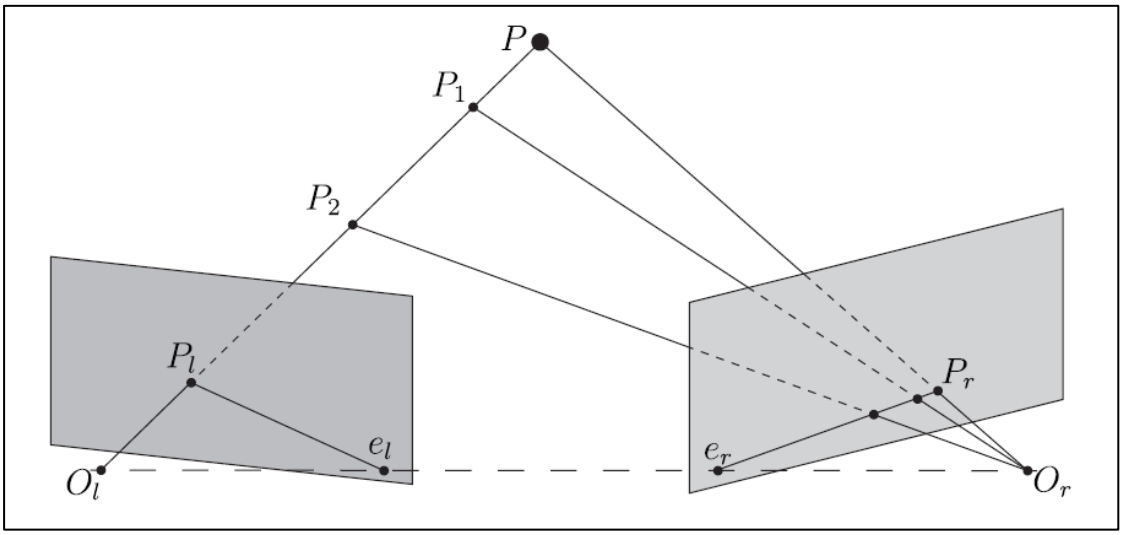

Figure 16- Stereovision Geometry (Guthrie, 2016)

To determine the three-dimensional coordinate of a point it is important to be able to find the same point, with a high location accuracy, in both image planes. The method of finding a point in both image planes is the major difference in stereovision algorithms.

Guthrie (2016) applies a metric over a subset window in the left image to describe a point using the sum of absolute difference (SAD) as the metric (OpenCV, 2018). The same window is passed over the right image to search for the same point. The window with the strongest correlation is likely to be the same point in the second image. Searching for the point across the whole image is computationally expensive and slow and may result in many false matches. Guthrie uses the concept of epipolar geometry, shown in Figure 16, to limit the search to a line search making the process more computationally efficient. The points e_l and e_r are the projection of the right projection centre O_r on the left image plane and the projection of the left projection centre O_l on the right image plane respectively. The points e_l and e_r are referred to as epipoles and the lines that connect P_l to e_l and P_r to e_r are epipolar lines which reduces the need from a global search to a line search. Once the feature P is identified in the

left image, it can be searched for along the epipolar line in the right image. The relative position of the cameras is used to rectify the images such that the epipolar lines run horizontally in the image as seen in Figure 17. Thus, a feature P projected onto row y_{P_l} on the left image should appear on the same row y_{P_l} on the right image. The feature P is projected onto column x_{P_l}in the left image and column x_{P_r} on the right image and the difference between these is known as the disparity. The disparity is measured in pixels and can be determined at sub-pixel locations depending on the algorithm used.

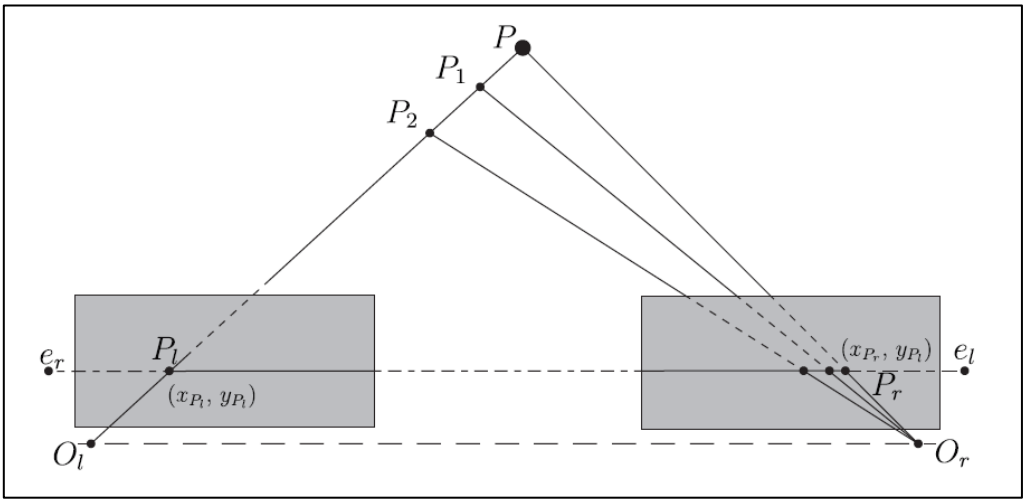

Figure 17- Stereo Rectification for Horizontal Epipolar Lines (Guthrie, 2016)

The pinhole camera model is an idealisation of a real camera. Real cameras contain distortion, discussed in more detail in section 1.5, which needs to be compensated for. It is also required to know the relative position between the two cameras. Calibration is used to remove distortion and to find the relative camera positions (OpenCV, 2018) necessary for image rectification. Any changes in the camera positions relative to each other would require a new calibration. Once the images are rectified the reference region in the left image is searched for along a horizontal (epipolar) line in the right image, as seen in Figure 18.

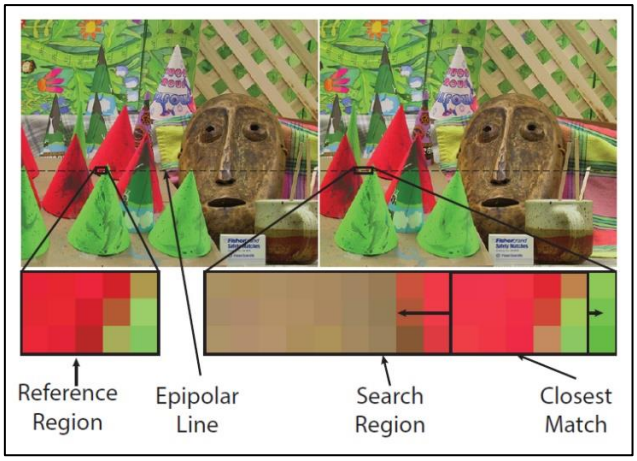

Figure 18- Subset Matching Along Epipolar Lines in Rectified Image Pair (Guthrie, 2016)

The camera geometry used by Guthrie (2016) enforces that the reference and search region are the same size and do not warp. If the cameras are placed wide apart the features in the left image will be appear very different in the right image in size and shape which affects the correlation. The algorithms are therefore most suitable for parallel, narrow baseline stereovision rigs.

For strain measurement it is necessary to determine the deformation of points from a reference to a current state. The reference state is assumed to be unstrained and the current state is the deformed state. The stereovision algorithm used by Guthrie (2016) needs the epipolar geometry to be known between views. The epipolar geometry is determined using the relative camera positions. The relative position and thus epipolar geometry can be determined once between the left and right images, at the reference or current image states, since the cameras are rigidly mounted together. However, the geometry between reference and current images cannot be determined easily. Thus, the algorithm used by Guthrie is not suitable for strain measurement where the deformation from one view to the next is to be measured and is not known beforehand, therefore the epipolar lines cannot be established. A more general algorithm is necessary that can search for points without knowing the camera position beforehand but an algorithm that does not require a global search as this is too computationally expensive.

1.4) Digital Image Correlation

In order to measure strain optically, the position of points on the tyre surface need to be measured accurately as the tyre deforms. Reference and current stereovision image pairs are used when matching points from the reference to strained state. The reference images denote a reference unstrained state. This does not imply that the object has zero strain but simply that the change in strain is measured relative to this state.

A general digital image correlation (DIC) algorithm can be applied to continuous and smooth surfaces which relies on a seed point, found using a global search, but thereafter points around the seed are found iteratively in a less computationally expensive manner eliminating the need for epipolar geometry. The Digital Image Correlation (DIC) algorithm uses subsets, analogous to the search region, to correlate unique features in a pair of stereo images (a sample of the images used in the tests are shown in Figure 19) namely:

- Left reference
- Right reference
- Left current
- Right current

The subset size is the size of window (in pixels) used to describe a feature. A subset window is used to match unique features in an image. All the image features are correlated relative to the left reference image. The unique features can be naturally occurring texture, or a speckle pattern applied to the surface but must be attached to the surface of the tyre to be able to measure strain in the surface of the tyre. The randomness of the pattern is needed to find unique features. The larger the subset the more unique the feature fingerprint is. The algorithm is applied to undistorted images, so the original images are cropped slightly and warped to remove camera distortions.

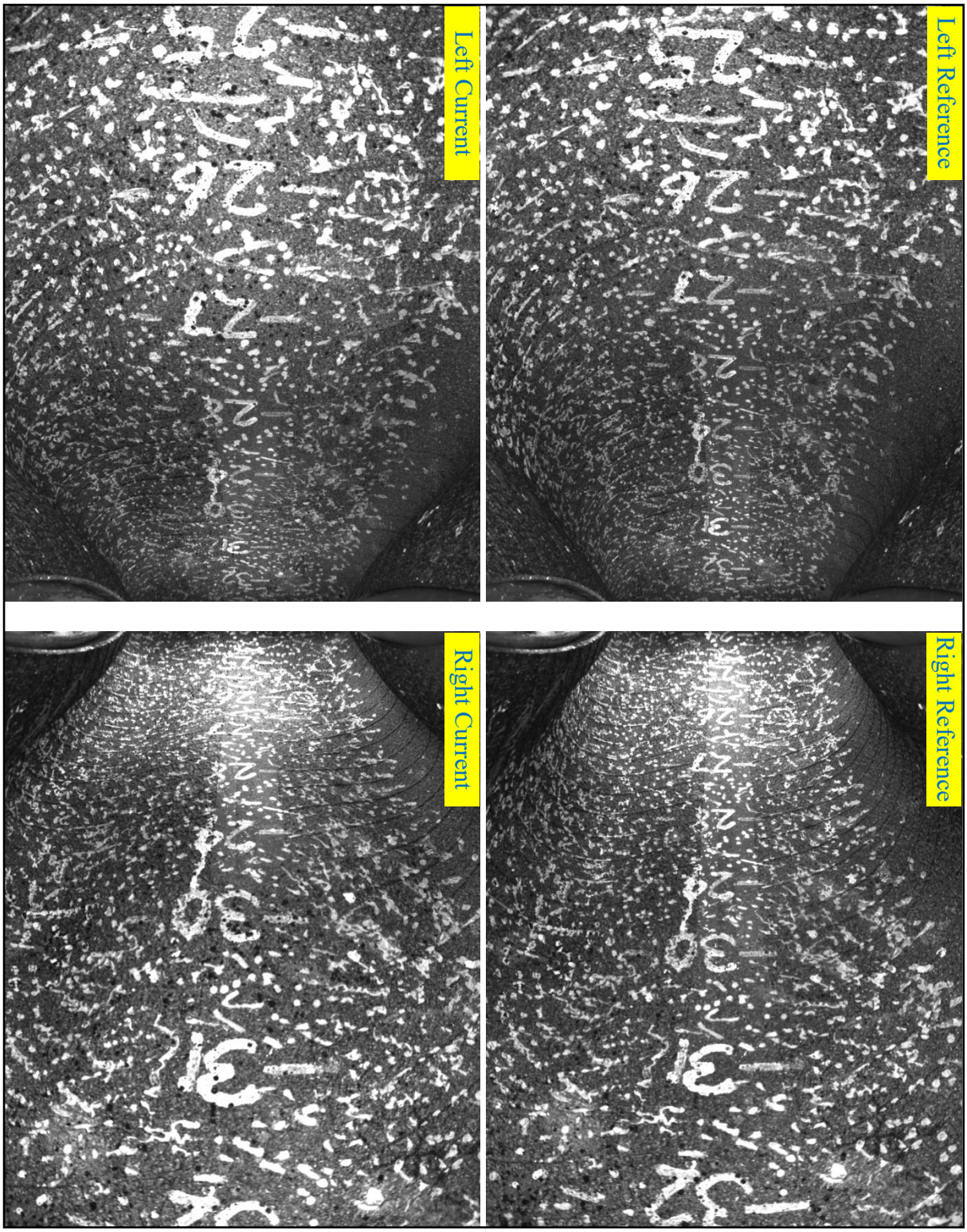

Figure 19- Raw Images Captured During 1.6Bar Tyre Vertical Loaded (100% Load Index)

With a narrow baseline setup, it is usually sufficient to use the same size and shape search window in the left and right image and just allowing for displacement along the epipolar lines. However, wider baseline setups can exhibit deformation between exact regions in left

and right images. Furthermore, the surface is strained between reference and current images. To make the algorithm suitable for the wide baseline and large strain application the subset can have vertical and horizontal displacement and can deform as well. The same algorithm is used to correlate left and right reference images as well as the left reference to left current image and left reference to right current image. The zero-mean normalized sum of squared difference (ZNSSD), Equation 3 (Pan, et al., 2013), is used as the correlation metric and allows for subset-deformation and displacement.

$$ZNSSD = \sum \left[\frac{f\left(x_{ref_{ij}}, y_{ref_{ij}}\right) - f_m}{\sum \left[f\left(x_{ref_{ij}}, y_{ref_{ij}}\right) - f_m\right]^2} - \frac{g\left(x_{cur_{ij}}, y_{cur_{ij}}\right) - g_m}{\sum \left[g\left(x_{cur_{ij}}, y_{cur_{ij}}\right) - g_m\right]^2} \right]^2 \quad (3)$$

Where $f\left(x_{ref_{ij}}, y_{ref_{ij}}\right)$ is the grayscale value in the reference image at pixel location $x_{ref_{ij}}, y_{ref_{ij}}$ and can lie between integer value for a very precise location i.e. sub-pixel location using bicubic interpolation . Where $g\left(x_{cur_{ij}}, y_{cur_{ij}}\right)$ is the grayscale value of the current image. f_m and g_m are the means of the subset in the first and second image respectively (left reference to right reference image, left reference to right current image or left reference to right current image).

If there is good correlation between features it is likely that the same feature has been found. The current image coordinates relate to the reference coordinates with Equation 4 and Equation 5.

$$x_{cur_{ij}} = x_{ref_{ij}} + u + \frac{du}{dx}\left(x_{ref_{ij}} - x_{ref_c}\right) + \frac{du}{dy}\left(y_{ref_{ij}} - y_{ref_c}\right) \quad (4)$$

$$y_{cur_{ij}} = y_{ref_{ij}} + v + \frac{dv}{dx}\left(x_{ref_{ij}} - x_{ref_c}\right) + \frac{dv}{dy}\left(y_{ref_{ij}} - y_{ref_c}\right) \quad (5)$$

Where $x_{ref_{ij}}, y_{ref_{ij}}$ is the location of a point (i, j) in the subset and x_{cur}, y_{cur} are the location of the subset centre. The subset-deformation vector $p = \left[u \quad v \quad \frac{du}{dx} \quad \frac{du}{dy} \quad \frac{dv}{dx} \quad \frac{dv}{dy}\right]^T$, which contains subset-displacement components as well as the gradients of the subset-displacement components, is solved for each subset. The subset-deformation vector is solved using the

iterative non-linear inverse compositional Gauss-Newton method (IC-GN) method (Baker and Matthews, 2001). The IC-GN method requires an initial guess close to the final answer to ensure convergence. In the algorithm described by Botha (2015) the same seed point, typically the strongest feature (unique feature fingerprint) in the image, is found in all images using a global search. The seed point serves as a starting point. Subset-deformation and translation of the seed point from the left reference image to the right reference image is determined. The subset-deformation and translation are also found for the seed point between the left reference to the left current image and for the left reference to the right current image. New points directly around the seed point are found using the IC-GN method with the seed point subset-deformation and translation as an initial guess. The actual subset-strain and translation of the new points (centres of the new subsets) is determined. Only subsets with a sufficiently strong correlation are used to avoid false matches. For each subset solved the correlation metric is stored from best to worst. The neighbouring points of the best correlated subset are found next. This ensures that the subsets are solved along the best possible propagation path. Subsets in the second image are correlated to a sub-pixel accuracy using bi-cubic interpolation. With subset locations known in all images, the subset centres are projected into a three-dimensional space using triangulation (Hartley and Sturm, 1997), based on the relative position of the cameras, to produce a point cloud with three-dimensional position and deformation. The positions and deformations of two or more points can then be used to numerically determine strain.

1.5) Camera Calibration

A calibration is needed to account for the deviations of a camera from the pinhole model and to solve for camera intrinsic and extrinsic parameters. The camera has intrinsic parameters, lens distortion and focal length, associated with the camera and lens combination. When using two cameras in a fixed stereovision rig the extrinsic parameters describe the positions and

rotations of a secondary camera relative to a primary camera coordinate system. Botha (2015) describes the main types of lens distortions as radial and tangential.

1.5.1) Radial Distortion

Radial distortion, as seen in Figure 20, causes the image to be warped especially near the edges of the image. The distortion is due to lens refracting rays near the edges of the image further than the rays close to the centre of the image.

1.5.2) Tangential Distortion

Tangential distortion is caused by the image plane not being parallel to the lens as seen in Figure 21.

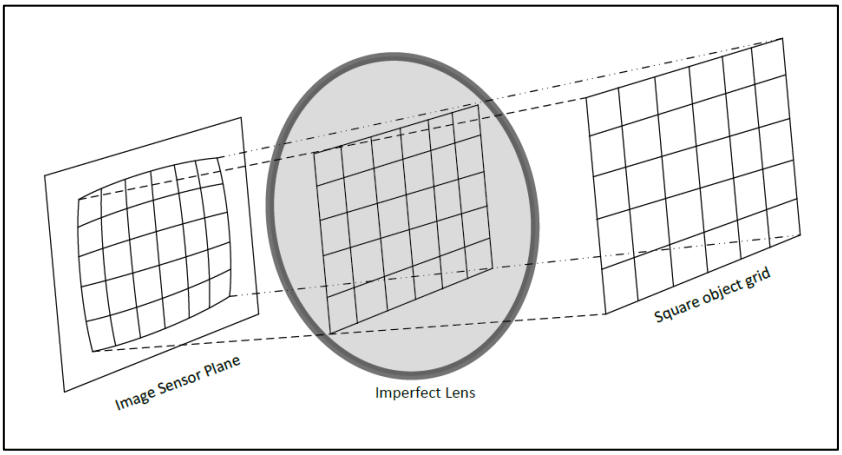

Figure 20- Radial Distortion (Botha, 2015)

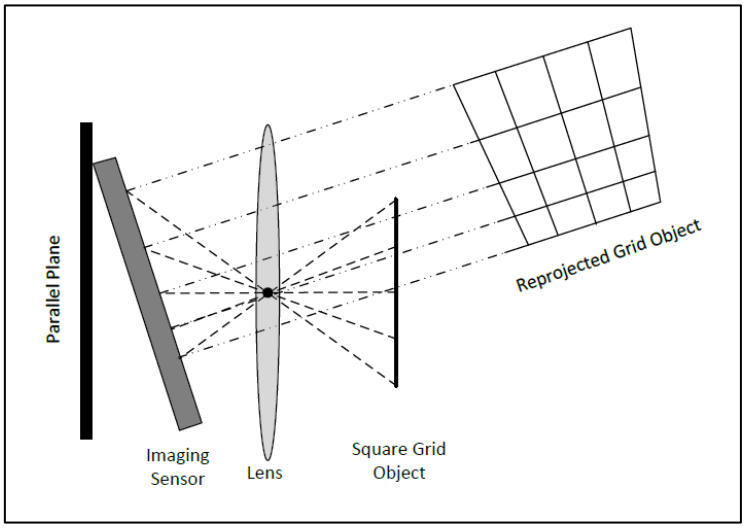

Figure 21- Tangential Distortion (Botha, 2015)

The cameras are calibrated using an algorithm based on common calibration practices as introduced by Zhang (2000) and using open source computer vision (OpenCV, 2018) libraries. Pictures are taken of flat surface with a known high contrast pattern using the cameras in their fixed positions.

Typically, a checkerboard or dot pattern on a flat plane is used. Multiple flat plane pictures need to be taken to solve for the unknown parameters. The surface is moved around and rotated randomly so that calibration pictures can be taken in the three-dimensional space where the surface can be seen by both cameras. Typically, between 10 and 20 pictures are taken covering all extreme positions and rotations that can still be captured by both cameras which is more than the minimum amount required to solve the parameters. The calibration algorithm uses a least squares approach to solve for all the parameters in the presence of noise. The relative nature of the calibration requires that a scaling be applied. The scaling is supplied in the form of a dimension measured on the surface pattern thus the calibrated rig does not require any post processing for scaling.

1.6) Conclusion of Literature Study

Stereovision techniques provide an ideal means to measure the shape, deformation and strain of a surface using non-contact means provided that a suitable DIC algorithm is used. The use of a mechanically stabilised camera measurement system inside the tyre allows for continuous measurement of the region of the tyre in contact with the terrain from the inside.

Chapter 2 will optimise the stereovision setup to improve on the positional accuracy obtained by Guthrie (2017) and determine the strain from the deformation measurement.

2) Stereovision for Strain Measurement Inside Tyres

Guthrie (2016) was able to capture many points on the inner surface of the tyre in the contact patch but with a low depth resolution and many lost points which would not be suitable for accurate and local strain measurement. This chapter addresses the changes made to the system to improve depth resolution and image quality necessary for the DIC algorithm to measure strain. The following changes and considerations are discussed:

- Camera Position
- Lighting Requirement
- Subset Size
- Speckle Pattern
- Calculating Strain from DIC Information

2.1) Camera Position

Dhond and Aggarwal (1991) presented a formula for the calculation of depth resolution as seen in Equation 6. The depth resolution (ΔZ) is optimised (depth resolution function is used as the cost function) to find the ideal position of the cameras in this stereovision rig. The depth resolution is a function of pan angle (φ), baseline (camera separation distance) (t) and distance to point (Z) as illustrated in Figure 22. Other factors that affect depth resolution but that cannot be easily changed or not necessary are set constant for the optimisation. These constants are minimum measurable disparity (Δd). The Δd is assumed to be 1, referring to 1 pixel. The sub-pixel interpolation in this study results in even lower minimum measurable disparity but 1-pixel accuracy can be used for a relative comparison to get the best geometry. The position in the image (x) is taken to be 0 referring to the centre of the image. The focal length (f), is determined from the calibration process.

$$\Delta Z = \Delta d \times cos^2(\varphi - \beta) \times (A - B) \quad (6)$$

$$\beta = \tan^{-1}\left(\frac{t - \left(\frac{Zx}{f}\right)}{Z}\right)$$

$$A = \frac{Z^2}{t \times f}$$

$$B = \frac{t}{f} \times \left(1 - \frac{Zx}{tf}\right)^2$$

A side by side setup limits the baseline of the cameras due to the space inside the wheel. It is proposed to place the cameras on opposite sides of the contact patch as can be seen in Figure 23. The depth resolution (ΔZ) is optimised (depth resolution function is used as the cost function) to find the ideal position of the cameras in this stereovision rig. The optimisation is subject to geometric constraints because the camera position is limited to within the tyre envelope.

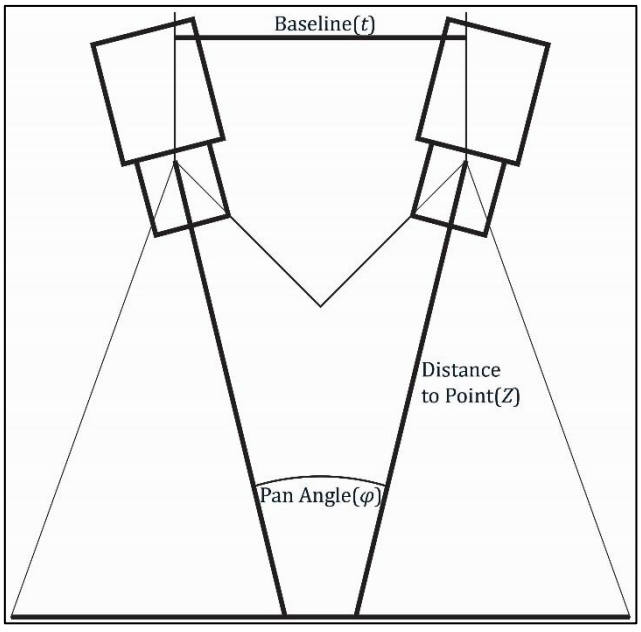

Figure 22- Parameters that Affect Depth Resolution

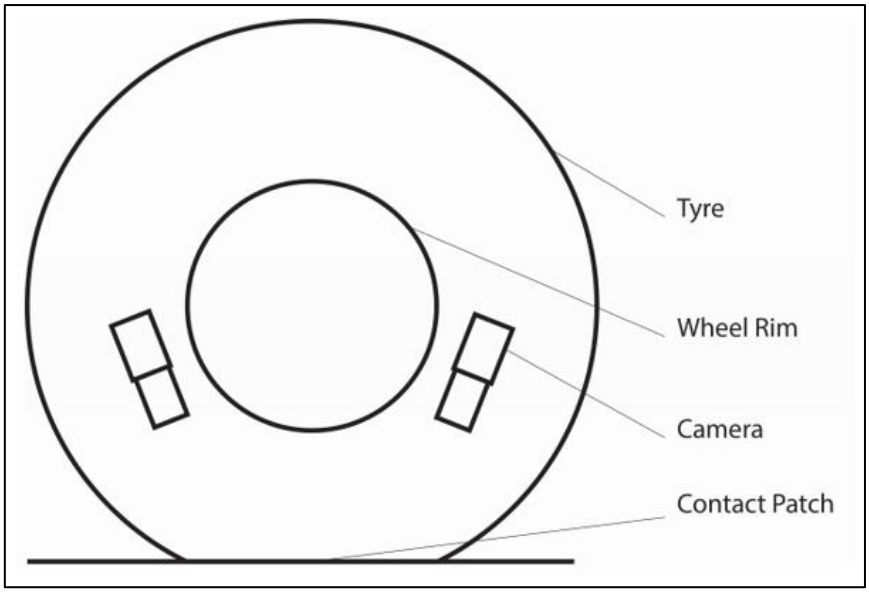

Figure 23- Proposed New Camera Layout

The viewing angle is required to set the geometric constraints. The viewing angle is a combination between lens (fixed focal length type) and camera and is experimentally measured yielding the results shown in Table 1. The viewing angle is determined through the centre line of the unrectified image in the horizontal and vertical directions. While rectification does crop the images slightly the cropping occurs near the corners where there is large distortion.

Table 1- Experimentally Determined Viewing Angles of Camera Lens Combination

Horizontal viewing angle	90.8º
Vertical viewing angle	78.83º

The system needs to be able to be able to capture the entire contact patch. A conservative contact patch is chosen to be 300mm long and 200mm wide (approximately A4 page size). The cameras are orientated such that the larger (horizontal) viewing angle captures the length of the contact patch while the smaller (vertical) viewing angle captures the width. The geometric constraints are applied such that:

- The cameras capture the entire patch length (seen in Figure 24 left).

- The trapezoid created by the camera is wide enough to capture the patch width (seen in Figure 24 left).
- The camera does not capture the rim in its field of view (seen in Figure 24 right).
- The cameras must lie within the tyre rim envelope.
- The cameras must be further that the minimal focus distance at the close end of the contact patch.

The problem is geometric therefore it is easy to choose a feasible starting point for the optimisation algorithm. A Sequential Least Squares Programming (SLSQP) algorithm which uses the Han–Powell quasi–Newton method is used. The SLSQP method is chosen for its easy implementation. The problem is geometric, so standard tolerances are sufficiently accurate. The problem quickly converges to a solution so no further methods are tested. Different starting points are chosen to ensure that the problem has converged to the global minimum. The depth resolution function is evaluated at points around the solution to ensure that the solution point is a minimum. The optimum position of the cameras and the theoretical depth resolution is shown in Table 2.

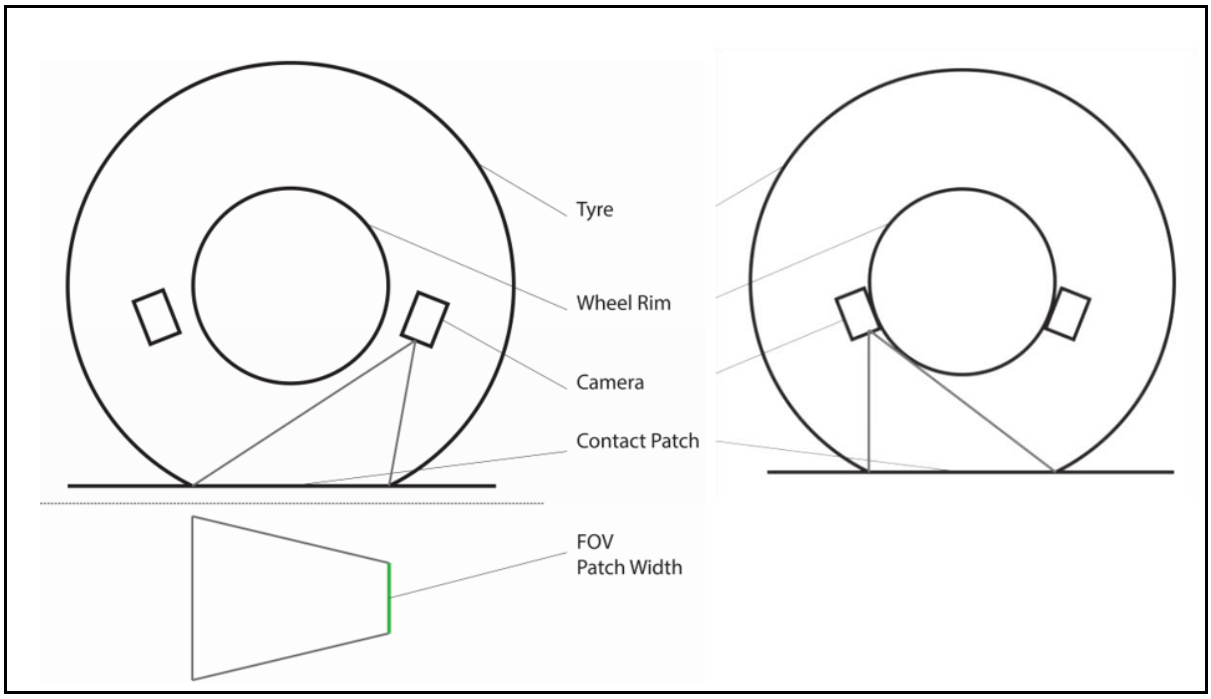

Figure 24- Geometric Constraints for Optimization of Camera Position

Table 2- Optimized Camera Position

Pan angle (φ)	1.0332Rad	or 59.2º
Baseline (Camera separation) (t)	0.3468m	
Distance to point (Z)	0.2308m	
Theoretical Depth Resolution (ΔZ)	0.0529mm	

Compared to the original side by side camera setup (Guthrie, 2016), the depth resolution of the new configuration has a theoretical factor of improvement of 26. The depth resolution is tested experimentally using a surface of known geometry. A pebble like surface is machined from an aluminium block and sprayed with a speckle texture, Figure 25.

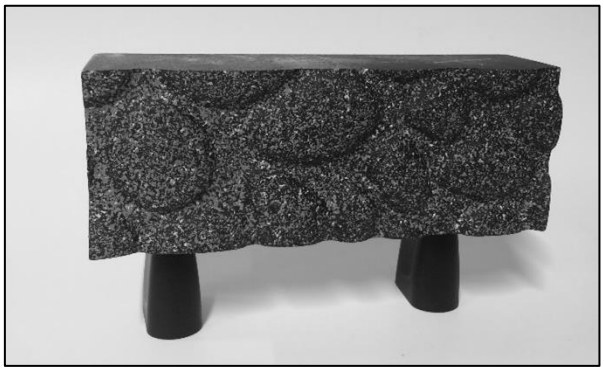

Figure 25- Surface of Known Geometry

The images are taken with the cameras in their original narrow baseline setup and the new wide baseline setup. The same DIC algorithm is applied to the images to create two point clouds of the surface. The point clouds are manually aligned to a rasterized form of the CAD model then automatically finely aligned using the iterative closest point algorithm (CloudCompare, 2015). The point to mesh distance, between the point cloud measured by the cameras and the mesh of the pebble surface, is then found for the original setup shown in Figure 26 and for the wide baseline setup in Figure 27.

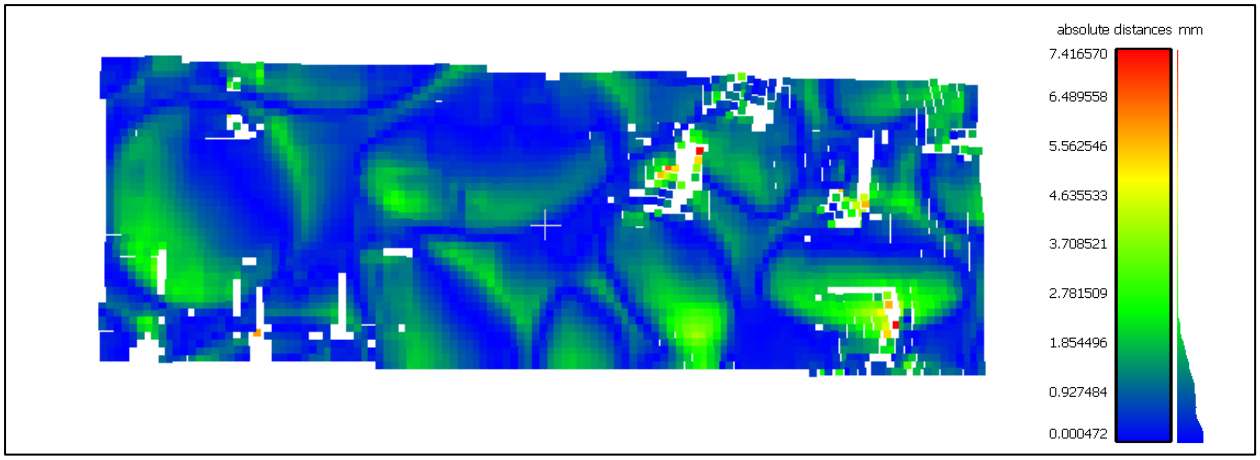

Figure 26- Distance of Points to CAD Model for Narrow Baseline

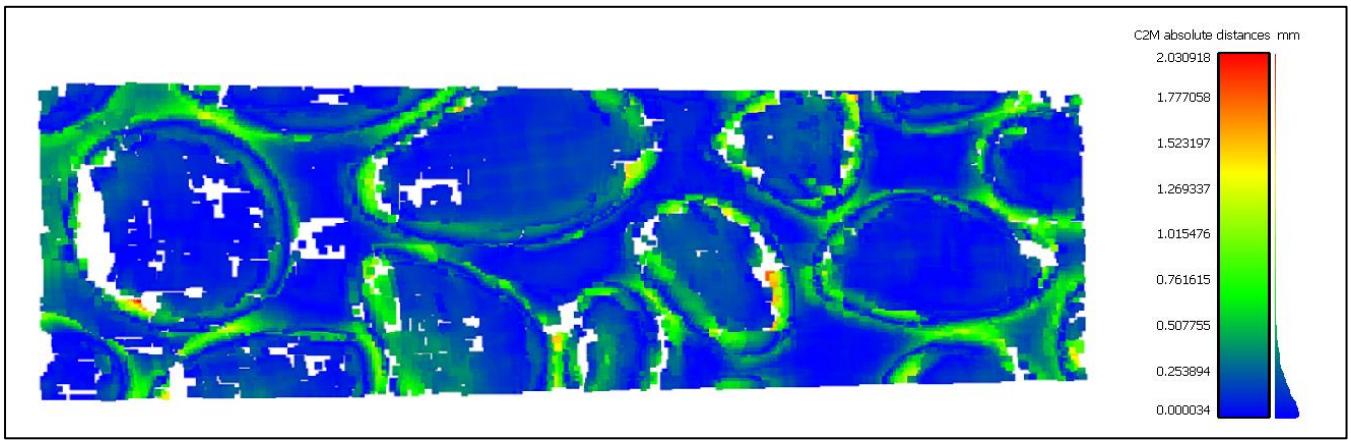

Figure 27- Distance of Points to CAD Model for Wide Baseline

The wide baseline can capture the base surface and the tops of the pebbles more accurately compared to the narrow baseline setup. The wide baseline loses accuracy at regions of high gradient as the algorithm expects uniform deformation for each subset which may affect the position of points when there are large changes in gradients in the surface. The inner surface of the tyre has a slowly changing gradient, so the subset deformation is fairly uniform. The CAD model is machined with a finite stepover which could have limited the experimental accuracy of the wide baseline setup. The error distribution, Figure 28, of the points is used to quantitively compare the two setups.

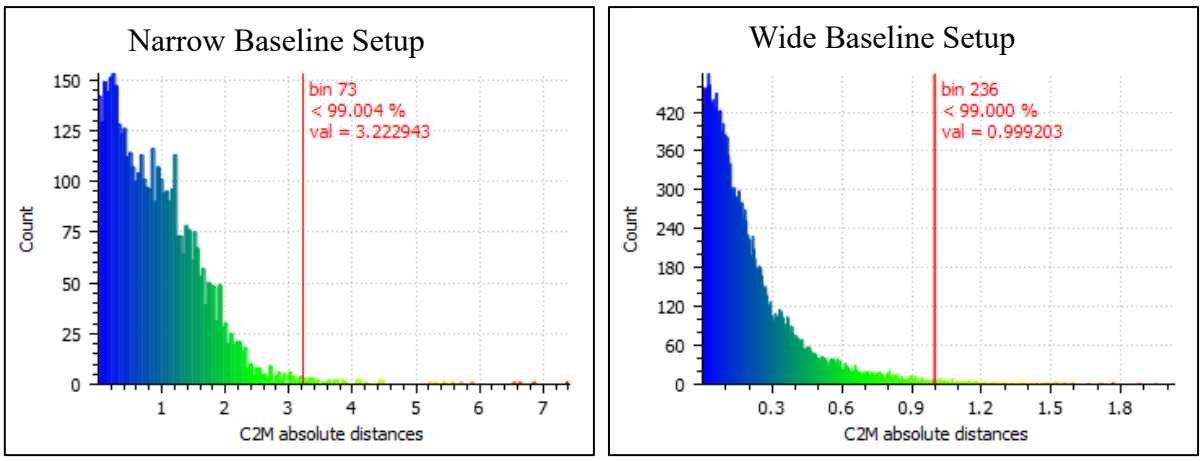

Figure 28- Distribution of Points for Narrow and Wide Baseline Setups

The 99% of points metric is used for experimental comparison of the two setups. In the narrow baseline setup 99% of points do not lie within 3mm of the model. In the wide baseline setup 99% of the points lie within 1mm of the model which suggests an improvement of at least factor 3. While this is less than the theoretical improvement, it is a substantial improvement and the new setup is used for the system. As noted, the surface is not ideal for the DIC algorithm and not fully representative of the inside of the tyre which would not have large gradient on the profile. Thus, higher accuracy can be expected on the tyre measurements.

2.2) Lighting requirements

The stereovision rig is used inside a sealed tyre. All the illumination is artificially supplied and therefore can be controlled. When capturing moving objects, it is necessary that there is enough light to create well exposed image but that the shutter time is short enough to avoid motion blur. There are many uncertainties and difficulties when modelling lighting such the amount of lighting power produced, the camera sensor and the reflectivity of the tyre surface, so an experimental approach is chosen to determine the lighting requirement. To determine the lighting requirement experimentally a relationship is found between supplied power and shutter time.

Ring lights are chosen to supply light from the view of the camera to avoid glare. In the stereovision setup points that are far away from the camera will be additionally illuminated by

the ring on the second camera for more evenly spread light. Neo-pixel ring lights are used in experimental work for their ease of implementation and their colour options but have limited power capabilities. The different colours are tested to exploit the efficiency of the camera sensor to certain light frequencies. No noticeable gain was noticed and the white LEDs on the neo-pixel rings proved to be much more efficient.

Guthrie (2016) explains that the cameras (PointGrey FL3-U3-13Y3M-C fitted with Kowa LM4NCL lenses) are chosen for the high speed and global shutter while maintaining a small package. The cameras have a resolution of 1280 by 1024 pixels and a maximum frame rate of 150 frames per second. The camera sensor converts light to electrical charge at each pixel location before it is converted to a digital value and stored as an image. With a global shutter, the entire sensor is exposed at the same time which is necessary when recording fast moving objects to avoid distortion. The camera has a shutter time and gain setting which are the only two camera settings that affect the lighting in the raw image. The shutter time sets how long the sensor is exposed to the light while the gain is the amount by which the electrical charge is multiplied by before it is converted to a digital value. The gain is set to middle of its operating range at G=10.023dB. The gain can be increased in low lighting conditions but results in increased noise. The rest of the settings such as brightness and contrast are post processing effects and are set to automatic to get a well exposed image as seen in Figure 29.

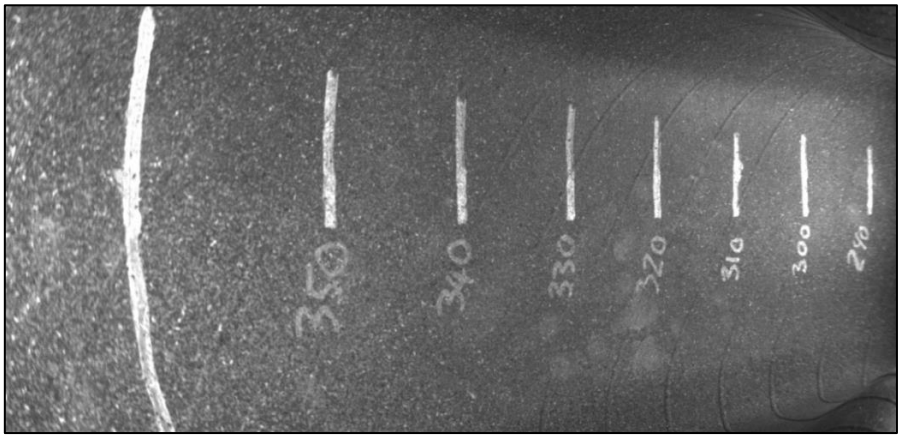

Figure 29- Well Exposed Tyre Surface Image (Cropped)

The cameras use fixed focal lenses which uses a combination of lenses to direct the light through a small opening onto the camera sensor. The fixed focal lens has two settings namely focus and aperture. The focus is set in the middle of the contact patch. The aperture controls the size of the opening and it is desirable to have a large opening to let in as much light as possible. It is also necessary that the points in the contact patch remain in focus. The depth of field (DOF) is the distance from the nearest point to the furthest point in focus. The required DOF for this application is extracted from the CAD model. The aperture is set, using the Equation 7 approximation, to let in the most possible light while maintaining a focus for the closest and furthest points in the contact patch region. The focal length (f), circle of confusion (c) and the distance to the surface (s) all need to have consistent units to be able to determine the aperture (N) measured in f-stops.

$$DOF \approx \frac{2Ncf^2s^2}{f^4 - N^2c^2s^2} \tag{7}$$

With the camera and lens set the lighting power can be varied and the shutter time can be measured. The lighting test is done in an unsealed tyre in a dark room to allow easy access to the cameras and lights. The test is done on a similar tyre as the actual test tyre was not available at the time. The lighting is incrementally increased on the neo-pixel rings. At each increment the camera automatically sets the shutter time to produce a well exposed image. The neo-pixel power consumption and camera shutter time at each increment is noted and used to produce Figure 30.

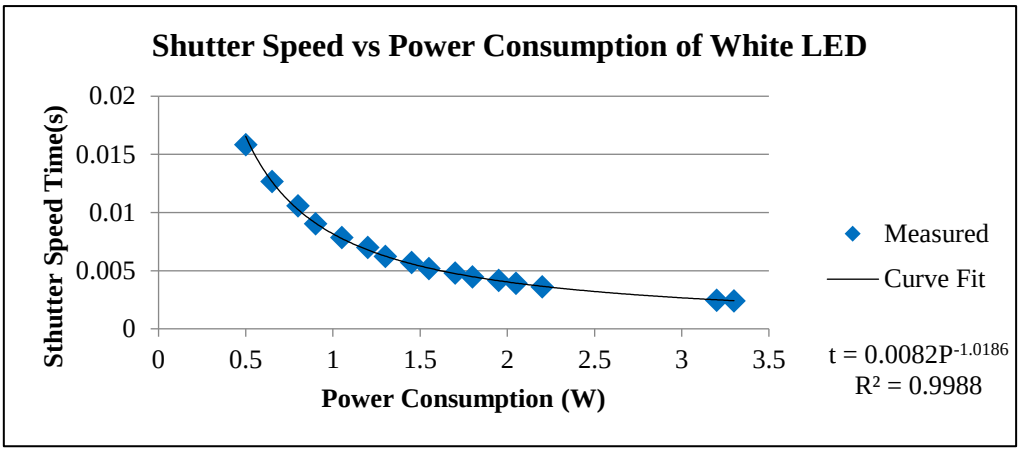

Figure 30- Shutter Time Power Requirement

An exponential curve is fitted through the experimental points (produced at each lighting increment). The Neo-pixel lights have limited power capability but demonstrate the inverse nature of the lighting in the system. The fitted exponential curve function is extrapolated to approximate the power requirement for a set shutter time. The test is not fully representative of the final setup and only serves to give an approximate power requirement. The discrepancies between the test setup and the final setup are the following:

- The tyre used in the test is not the same as the tyre for the final setup.
- The speckle pattern on the inner surface of the test tyre is slightly different and may affect the amount light reflected to the cameras.
- The test setup does not include the rim which would increase the amount of light reflected to the cameras.
- The Neo-pixel lights in the test setup may not have the same efficiency as the LEDs chosen for the final setup.
- The lighting power is the amount of power that the neo-pixel rings draw and not the actual amount of light supplied.

The required shutter time is chosen based on the required vehicle speed. To prevent motion-blur the tyre may not move more than one pixel while the image is being taken. The pinhole camera model can be used to relate the pixel size to distance on the road with a correction for the pan angle as seen in Equation 8.

$$x = f\frac{X}{Z} \times \cos(\frac{\varphi}{2}) \tag{8}$$

$$X = \frac{(4.8E-6)(0.2308)}{(3.5E-3)} \times \frac{1}{\cos(\frac{1.0332}{2})}$$

$$X = 3.64 \times 10^{-4}\ m$$

At a speed of vs=40km/h (maximum speed of the agricultural type tyre used) the required shutter time is determined using an approximation of the fitted trendline function Equation 9.

$$t \approx 0.0082P^{-1} \tag{9}$$

$$P \approx 0.0082(\frac{3.64E-4}{40 \div 3.6})^{-1}$$

$$P \approx 250W$$

The Neo-pixel LEDs have limited power and are replaced with more powerful custom white LED rings. The combined power rating of the LEDs on both LED rings is 300W which is enough illumination for testing up to 40km/h. A constant 300W supply of power would heat up the tyre very quickly which would affect the performance and behaviour of the tyre. It is therefore necessary to strobe the LEDs to be on while the camera is taking a photo and off between photos. A custom microcontroller board is developed to use the trigger signal from the camera and produces a pulse that turns the LEDs on. The microcontroller is used to set the width of the pulse which dictates how long the LEDs are turned on. A custom LED driver board is used to power the LEDs from a higher voltage source than the logic level voltage created by the microcontroller board using MOSFETs for fast on/off switching.

2.3) Subset Size

The subset size is the size of window (in pixels) used to correlate features in an image. The larger the subset size the more unique patterns can be found in the speckle pattern giving a more unique feature fingerprint to the subset. The unique feature fingerprint, found in the left reference image, allows for good correlation of the subset to other similar subsets in the other images namely right reference, left current and right current.

A large subset size also provides better sub-pixel location accuracy as shown by Hild and Roux (2006). The setup described by Hild and Roux (2006) also uses a 1024 by 1280 pixel resolution in a classical single camera DIC approach. Hild and Roux (2006) changes subset size and measures the displacement uncertainty of the feature, the displacement uncertainty is displayed in Figure 31.

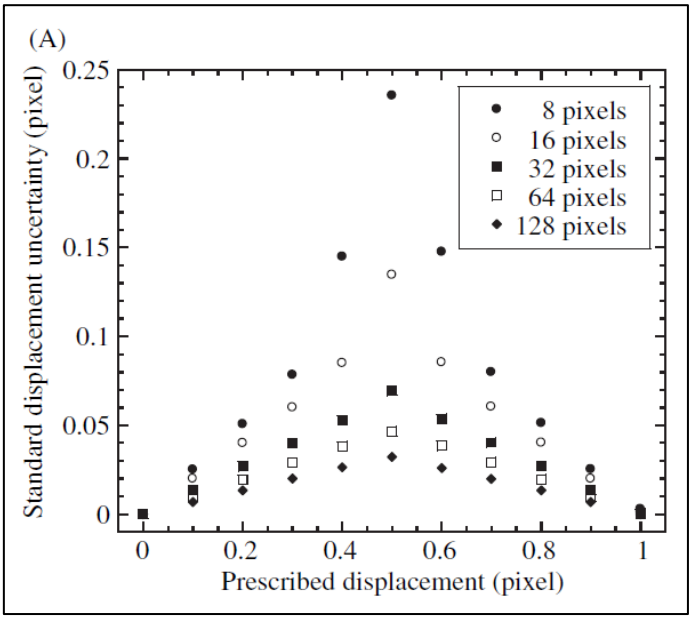

Figure 31- The Effect of Subset Size on Displacement Uncertainty (Hild and Roux, 2006)

In the algorithm used by Hild and Roux (2006), the position of a point is interpolated to a sub-pixel accuracy to improve displacement measurement much like the algorithm used by Botha (2015). If the point lies near or on the pixel there is little or no uncertainty on the displacement. At locations between pixels the uncertainty is large (about 0.24 pixel uncertainty for a 8 pixel subset). By increasing the subset size, the uncertainty can be decreased to about 0.05 for 64 pixel subset. While the tests presented by Hild and Roux (2006) are for a single camera the results are applicable to the stereovision rig presented in this paper which has the same camera resolution. Increasing the subset size will result in much less displacement uncertainty on the image plane at point located between pixels and thus less uncertainty on the position of a point.

The subset size cannot be increased indefinitely because larger subsets require more memory and time to process. Another drawback is the assumption of a uniform subset-deformation over the subset window, which is assumed by the algorithm used by Botha (2015) to improve correlation as seen in Figure 32.

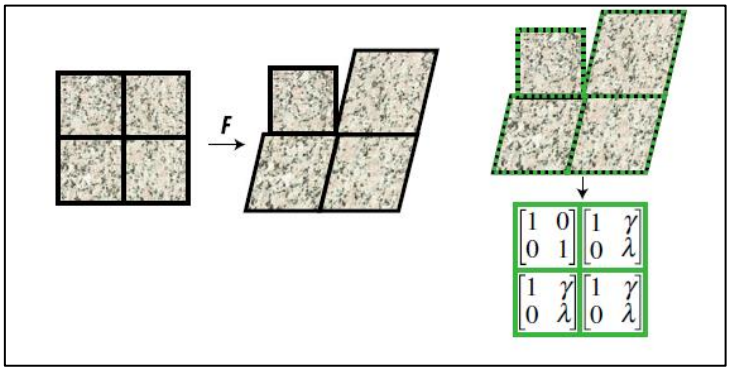

Figure 32- Deformation of Subsets (Boyle, et al., 2014)

In reality the points in the subset do not deform uniformly over the subset. Points further from the centre that do not have the same deformation decrease the possible correlation. Regions that do not have smooth deformation may get lost due to a large decrease in correlation caused by points far from the centre. The subset size should be chosen such that a large enough window is used to be able to uniquely and accurately measure points while being small enough to not span large changes in deformation to lose correlation.

In this study a subset size of 45 is used for most of the tests as this value gives good results for most of the tests where the deformation is not too large. Pan, et al (2013) uses a subset of 41 in tests that use a very similar algorithm. Some tests in this study have large subset deformations which results in many points being lost. In this case the subset size is increased in increments of 4 until a sufficient number of points are captured.

2.4) Speckle Pattern

The wide separation requires special care to be taken when applying the speckle pattern. The spray paint droplet speckle pattern as used by Guthrie (2016) is not suitable for such wide baseline setups. The features that are close and large in the one image are far and small in the

other image causing a weak correlation with small speckles which may no longer be visible when far from the camera. There is no evaluation of speckle for wide baseline camera setups in literature however Crammond, et al (2013) offers results for high accuracy, small strain applications. Crammond (2013) generates speckle patterns of varying speckle radius and varying amount of speckles per 128 by 128 pixel subset. Examples of two patterns are shown in Figure 33.

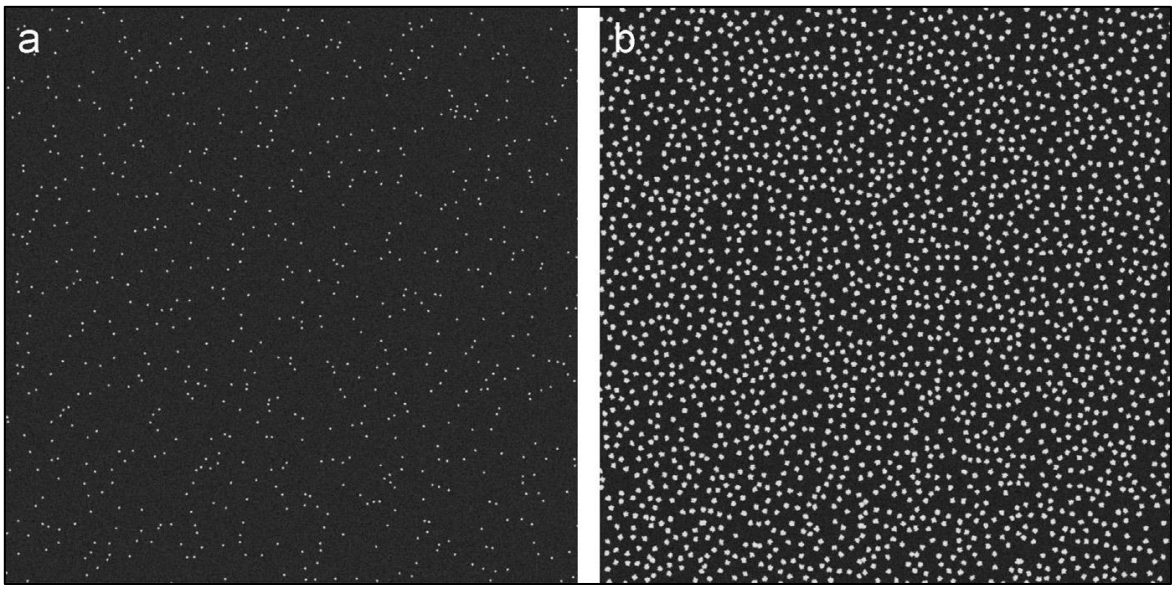

Figure 33- Examples of Different Speckle Patterns (Crammond, et al., 2013)

It is desireable to have large amounts of randomness and unique patterns in each subset but there is a finite limit due to the number of pixels in the subset so a tradeoff is needed. This tradeoff is demonstrated by Crammond in his computer generated speckle patterns. The speckle pattern are then artificially strained and DIC is used to extract the amount of strain. The standard deviation between the imposed strain and the DIC measured strain of each point is used to evaluate the speckle as seen in Figure 34.

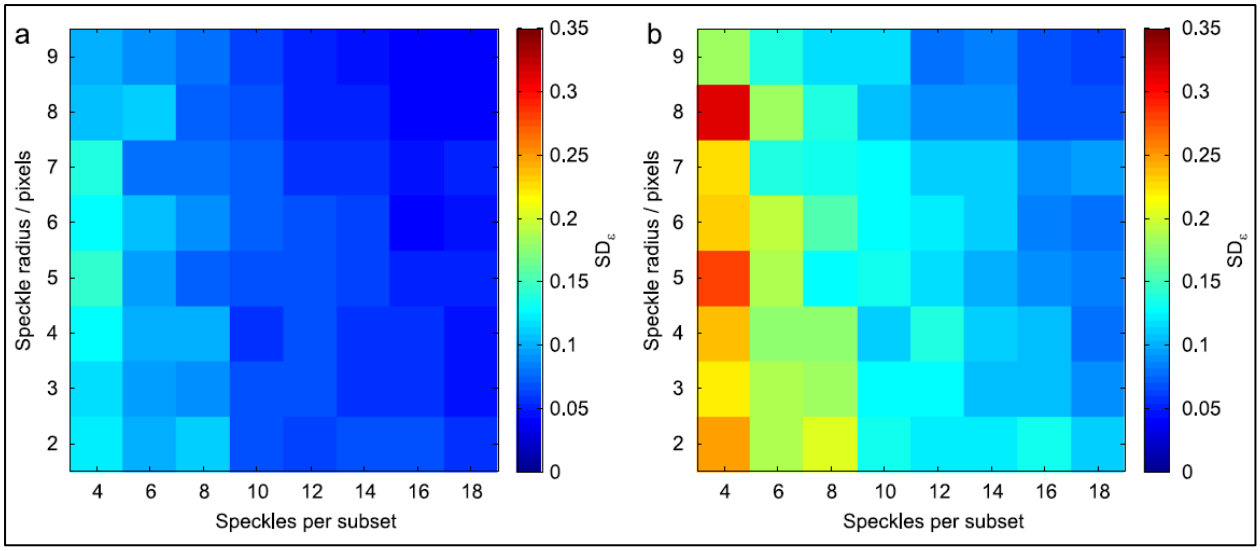

Figure 34- Evaluation of Various Speckle Pattern for 1% Strain (Left) and 2% Strain (Right) (Crammond, et al., 2013)

It is seen from Crammond, et al (2013) that results, that have a higher number of speckles per subset and larger speckle size, produce smaller deviation of DIC points. It should be noted that this result is for a single camera with small strain amounts (1 and 2 percent) with 128 by 128 subset on a 1408 by 1408 image. This idea is applied to the wide baseline setup when applying the speckle pattern to the tyre and the correlation between the left image and right image is used as a metric to evaluate the speckle pattern. A spray paint droplet speckle would not be suitable as is usually used due to the size of the speckle needed. Instead a 2.3mm white paint marker is used to create random dots and short lines on the underlying black surface. The marker is suitable as dots can still be seen in the image at points far away from the camera. The ZNSSD correlation for different stages of speckle application is shown in Figure 35 alongside the speckle pattern as seen from the left camera. The correlation is slightly cropped (the correlation uses the undistorted images and is cropped further due to the subset size near the edges) and should not be directly compared to the image but instead to other correlations. The darker the colour in the correlation image the better the correlation of points.

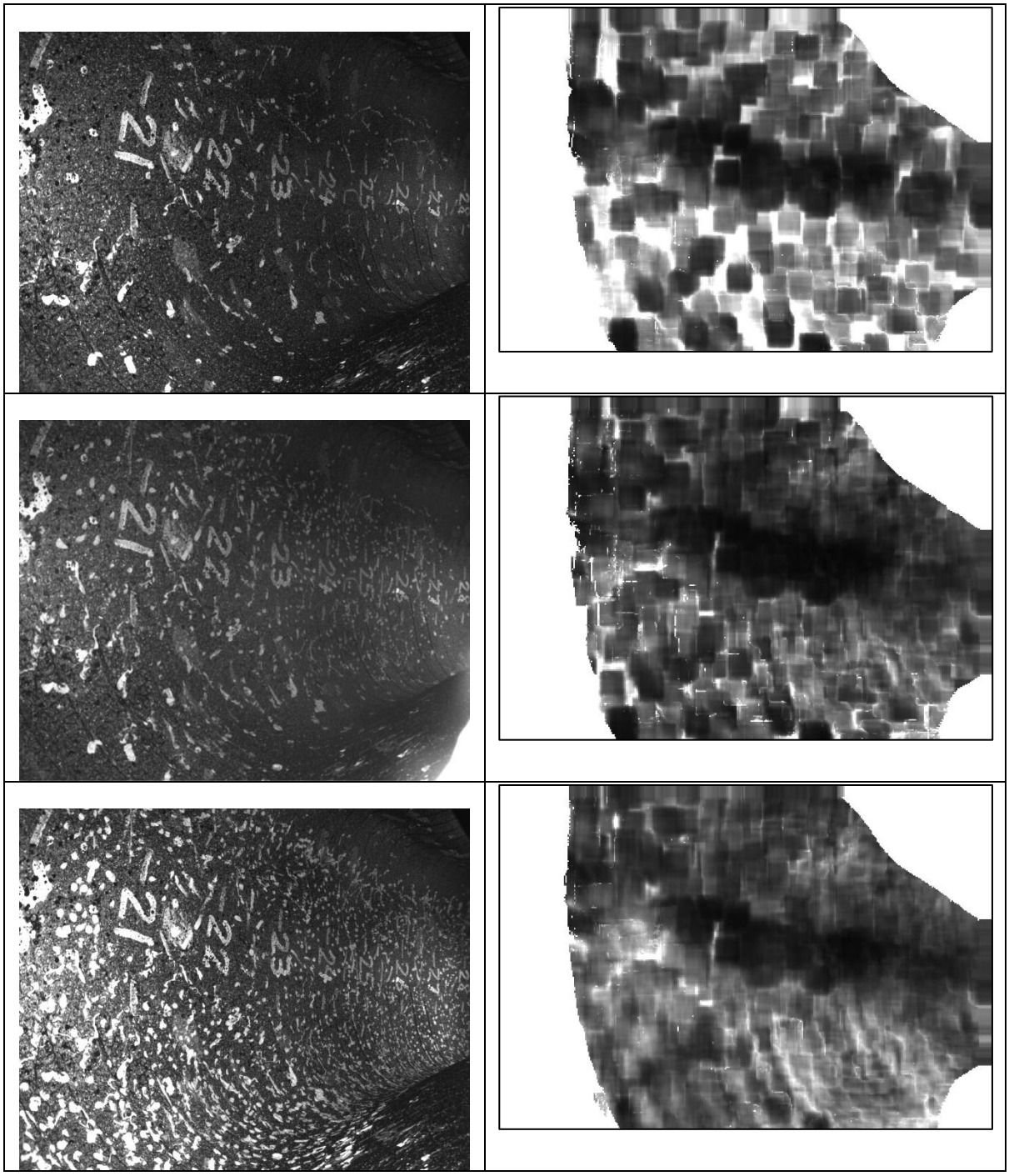

Figure 35- Different Speckle Patterns and Associated Correlation

The images were all processed with the same settings but the exact position of the tyre changes slightly due to unavoidable bumping of the tyre caused when creating the speckle pattern. As the number of points in the speckle increases, the correlation improves. Since the process of increasing speckle is not easily reversed, the process was repeated until there was no significant improvement. There is a large increase in the number of speckle points between

the second and third image but only a small improvement in the correlation. The second correlation picture does have some dark patches of good correlation, but the smooth nature of the third correlation is preferred as it results in more points found on the left edge of the correlation. The correlation can be improved further by changing the subset size, but this requires more processing time and memory therefore only a relative comparison is done for determining the best speckle pattern. The white speckle points reflect light better than the black tyre surface and an increase in speckle points decreases the lighting requirement so that even shorter shutter times are possible.

The images are well exposed and evenly illuminated for the standard undeformed tyre image. As the tyre deforms the illumination varies as the tyre surface moves closer to the camera or as the tyre angles to reflect light from the light source. The quality of the images is affected as black regions become more grey affecting the appearance of the speckle pattern and therefore the correlation between the two images decreases. The effect is particularly important on the wide baseline stereovision rig as bright regions in one image may appear dark in the other image due to large difference in distance from the camera to the surface. The images are therefore processed, to improve the appearance of the speckle pattern, before they are used in the DIC algorithm. The image is represented by a matrix of values ranging from 0 (black) to 255 (white). A subset window is passed over the image, without any overlap, finding the minimum and maximum value in each region to be used at the region centre. The values are linearly interpolated between regions so that the appearance of the speckle pattern is not affected. Each pixel is then rescaled on a new colour scale, indicated in Figure 36, where the minimum for the region is 0 and the maximum for the region is 255. This is suitable for regions where there is a speckle pattern as the minimum corresponds to the black of the tyre surface and the maximum corresponds to the white of the speckle. The method does not work well at

regions with no speckle as there is no dynamic range and the rescaling is poor however no points are expected here so the flaw is ignored.

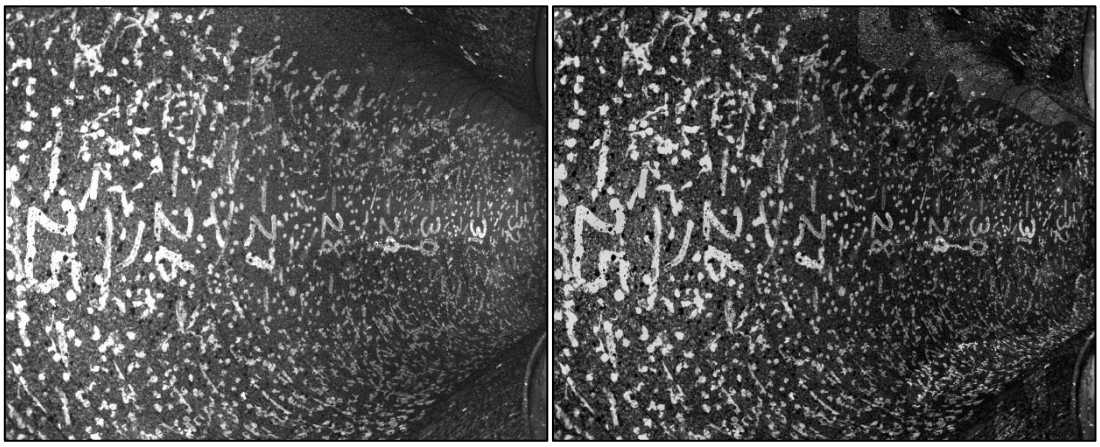

Figure 36- Raw Image (left) and Colour Rescaled Image (right)

2.5) Calculating Strain from DIC Information

Strain is the ratio of the amount deformation to an initial dimension. The DIC algorithm is a general high precision algorithm used to correlate subsets across images. The DIC algorithm requires 4 images, left and right reference images and left and right current images. The algorithm produces a point cloud of unique points found on the inner surface of the tyre with three-dimensional positions and three-dimensional deformation. The deformation and position can be used to determine the strain in the surface of the tyre. It not possible to determine deformation through the thickness of the tyre as there are no points available other than the points on the inner surface. Strain measurement is therefore limited to two-dimensional surface strain.

The simplest two-dimensional element is a constant strain triangle (CST) as shown in Figure 37.

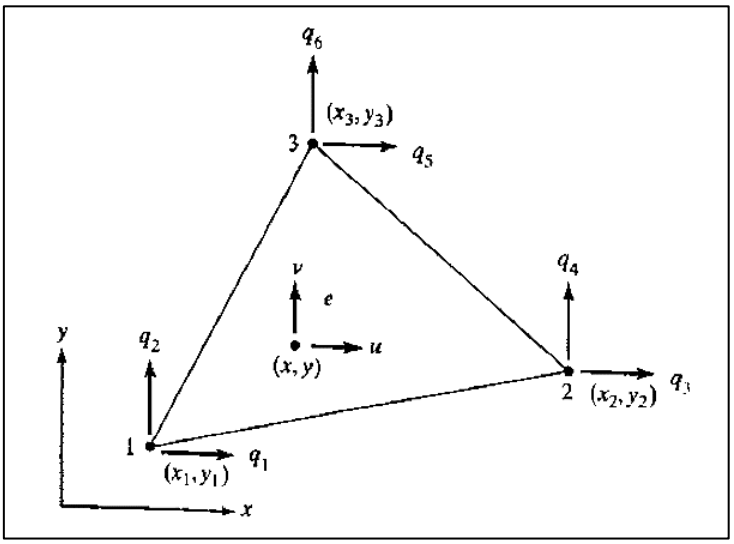

Figure 37- Constant Strain Triangle Element (Chandrupatla and Belegundu, 2012)

The CST element has three nodes each with two degrees of freedom (x_n, y_n) each. The points obtained from the inner surface of the tyre have global three-dimensional coordinates relative to the cameras. It is necessary to create a two-dimensional coordinate system for each CST to limit the deformation to two dimensions. This coordinate system is defined by the plane which goes through all three points of the triangle. Any three points found on the inner surface of the tyre can be used to create a CST. On the inner surface of the tyre, the strain at each point can be determined, using standard equations, in the lateral and longitudinal direction by applying CSTs to the surrounding points. Strain at a point is taken as the average lateral and longitudinal strain of the four triangles created around the point as seen in Figure 38. The figure shows that the three points to not necessarily be adjacent to one another and can be further apart to reduce noise.

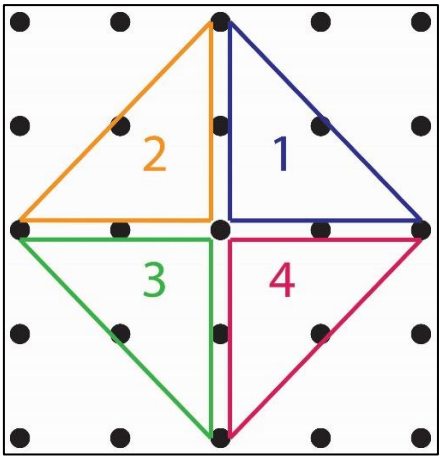

Figure 38- Four CST Triangles Around a Point

For each triangle a local plane is created that passes through all three points with the z axis normal to the plane. The x and y axis lie on the plane such that the x-axis has no y-component when projected on the global axis system of the camera. Similarly, the y-axis has no x-component when projected onto the global axis system. Local coordinates are created for each point to reduce the points to two-dimensions in x and y. The local coordinates are used in standard formulas (Chandrupatla and Belegundu, 2012) to determine the strain in the triangle according to Equation 10.

$$\begin{Bmatrix} \varepsilon_x \\ \varepsilon_y \\ \gamma_{xy} \end{Bmatrix} = \frac{1}{2AT} \begin{bmatrix} y_{23} & 0 & y_{31} & 0 & y_{12} & 0 \\ 0 & x_{32} & 0 & x_{13} & 0 & x_{21} \\ x_{32} & y_{23} & x_{13} & y_{31} & x_{21} & y_{12} \end{bmatrix} \begin{Bmatrix} u_1 \\ v_1 \\ u_2 \\ v_2 \\ u_3 \\ v_3 \end{Bmatrix} \tag{10}$$

Where ε_x and ε_y are the longitudinal and lateral strain respectively, AT is the area of the triangle. x_{nm} is the difference between the x coordinate of point n and m. y_{nm} is the difference between the y coordinate of points n and m. u_n and v_n is the deformation of the n^{th} node in the longitudinal and lateral directions respectively. The lateral and longitudinal strain at the point is taken as the average lateral and longitudinal strain of the four CSTs.

The stereovision rig has many factors which contribute to the strain accuracy. To evaluate the ability of the rig to measure strain, the results of the DIC measurement need to be

compared to an actual strain. The easiest implementation of strain evaluation is to artificially create a known strain in an image. A speckle image is used as reference image. The speckle is artificially strained in the longitudinal direction to produce 1% and 8% strained speckles. Figure 39 shows the unstrained speckle image as captured by the left camera with colour overlay showing the unique points found.

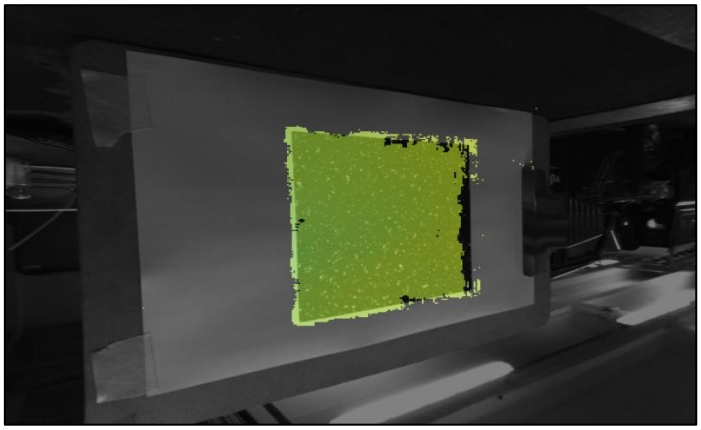

Figure 39- View of Speckle Showing the Points Captured

The test does not use the same speckle pattern as the tyre, and this may slightly affect the performance of the algorithm. The algorithm should be able to account for translations, rotation and deformations therefore the two images are not aligned, and the flatness of the paper is not checked. The longitudinal and lateral strain of the points is shown for 1% and 8% strain in Figure 40.

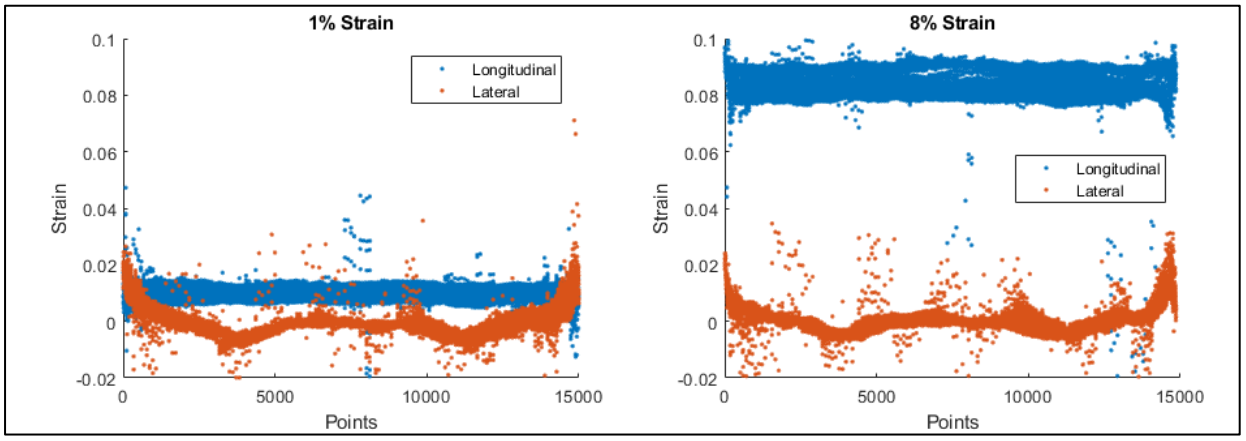

Figure 40- 1% and 8% Longitudinal and Lateral Strain

The means of the points are as expected. The mean of lateral strain appears to be near zero for both cases. The longitudinal strain lies at about 1% and about 8% respectively. The absolute accuracy of the printed strain is not exactly known and depends on the printer scaling. The two chosen strain values are used to illustrate that the system will be able to measure at least strains as low as 1% and as high as 8%. Except for outliers, the points seem to fit in a 0.5% noise band. The noise band can be visualised in Figure 41, which plots the strain as a colour overlaid over the points.

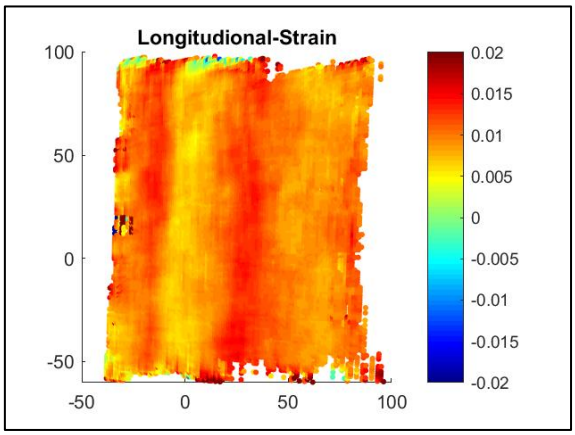

Figure 41- Longitudinal Strain Measured on 1% Deformed Speckle

The printed speckle pattern image is not the same as the speckle pattern to be used on the tyre. The speckle image is printed on paper which does not have the same reflective properties as black rubber and is not easy to achieve even illumination. As a result, a large subset size needs to be chosen to uniquely identify points. With large subset size and relatively fine speckle points further from the centre do not deform uniformly, as assumed by the algorithm, and cause a shape mismatch which affects the accuracy of the algorithm (Su, et al., 2019).

3) Contact Patch Strain

Chapter 2 concluded that the strain measurement system is able to measure planar strain on a surface with good accuracy and taking into account out of plane effects. This chapter describes the test setup used to measure strain in the tyre contact patch with different applied loading conditions.

3.1) Experimental Test Setup

3.1.1) Test Tyre

Green (2011) did strain measurement on a road tyre which only experiences small strains, due to the homogenous tread pattern. The small strains are difficult to measure in the presence of noise. Green loaded the tyre using deflection and not force measurement. It is not known whether these deflections correspond to realistic loading on the tyre. The results from Green showed a more homogeneous strain field with gradually reducing strains. An agricultural tyre with large tread blocks is expected to create strain concentrations which will result in more pronounced strains compared to measurement noise. The Trelleborg TM700 280/70R16 TL (inflation pressure table (Trellerborg AB, n.d.) shown in Figure 42 and tyre shown in Figure 43) tyre is used for the tyre testing process.

TM700

Size	Load-Index/ Speed Symbol	psi bar	9 0,6	12 0,8	17 1,2	23 1,6	29 2,0	35 2,4	43 3,0
		Km/h				Kg/Tyre			
280/70R16 TL	112A8 (112B)	**40 S** 10 HT S	580 620	640 680	760 810	880 940	1000 1070	**1120** 1200	1900 H (#)

Figure 42- Inflation Pressure Table

Figure 43- Trelleborg TM700 (Trellerborg AB, n.d.)

The agricultural tyre has a high profile which should result in large deflections. The tread blocks are relatively stiff compared to the rest of the tyre. This non-homogeneous tyre profile is expected to cause interesting phenomena in the contact patch region. It is expected that the tread pattern will be evident in the produced strain fields. A passenger vehicle tyre has relatively homogenous tread pattern and a relatively stiff belt. One will therefore not expect to see the effect of the tread on the strain field on the inside of the tyre.

3.1.2) Static Tyre Test Rig

The testing will be done in a controlled environment on a static tyre test rig. The static tyre test rig is shown in Figure 44.

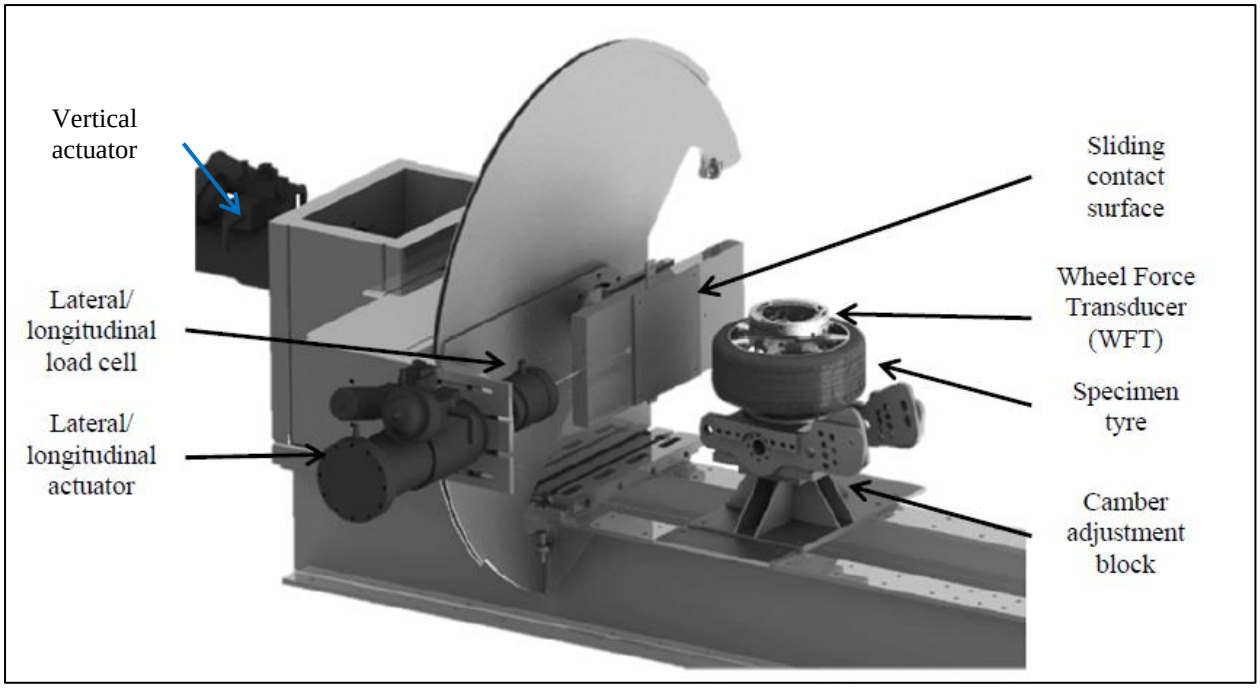

Figure 44- Static Tyre Test Rig Positioned for Longitudinal Test (Wright and Els, 2017) (modified to include vertical actuator)

The test rig is capable of testing very large tyres with the wheel mounted horizontally on the static mounting block. The wheel is locked preventing it from rotating. The road surface, represented as a flat steel plate, is actuated by a vertical and lateral actuator. The road surface, along with lateral actuator, can be rotated using a winch up to 90 degrees for aligning moment tests. Once rotated to 90 degrees the lateral actuator can be used for longitudinal tests. The test rig does not have any feedback-based control system built in and no force limiters, but rather is displacement based. Lasers are used to determine the vertical and lateral displacement.

3.1.3) Wheel Force Transducer

The forces are measured at the centre of the wheel using a wheel force transducer (WFT) shown in Figure 45.

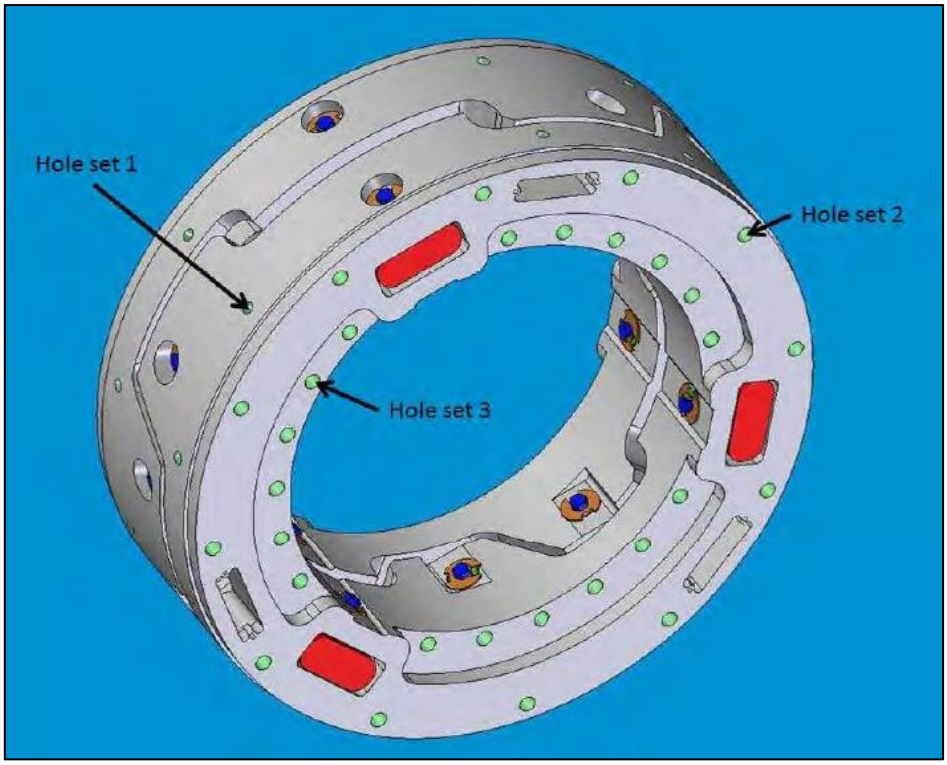

Figure 45- 6-Axis Wheel Force Transducer (Els, 2012)

The wheel force transducer uses 6 load cells to measure all forces and moments at the centre of the wheel. The measurements from the 6 load cells are uncoupled and converted to forces using a calibration file.

3.1.4) Data Acquisitioning System (DAQ)

The wheel force transducer connects to a dedicated data acquisitioning system for measuring the forces. The DAQ is accessed through a laptop computer. A second data acquisitioning system is used for measuring the vertical and lateral laser displacements as well as the pressure in the wheel.

3.2) Testing Procedure

The in-tyre camera system and the externally based DAQ are not synchronised with a trigger. The in-tyre camera system is only accessible over wireless network which makes it difficult to synchronise with external systems. This limits the tyre testing to quasi-static type tests where data from the different systems is lined by sample number. Tests were performed in a slow incremental manner taking samples at each displacement increment on each device

(WFT, DAQ, T2Cam). The test setup is shown in Figure 46. The quasi-static nature of the tests ensures that there are no thermal effects. Four tests were performed namely:

- Inflation Test
- Vertical Load Test
- Lateral Displacement Test at Different Vertical Loads
- Longitudinal Displacement Test at Different Vertical Loads

Figure 46- Test Setup on Static Tyre Test Rig

3.2.1) Inflation Test

The effect of any external loading on the contact patch strain remains largely unknown. The inflation test has no external loading and can be compared to the strain of a pressure vessel. Therefore, the inflation test is used as a validation test to partially prove that the strain measurement system works. The tyre is inflated from 0Bar to about 3Bar. The strain is calculated relative to an uninflated tyre. The strain in an area the size of the contact patch, at the highest pressure (2.94 Bar), is shown in Figure 47. The data in the region from 64mm to 66mm, on the lateral axis, is highlighted in black.

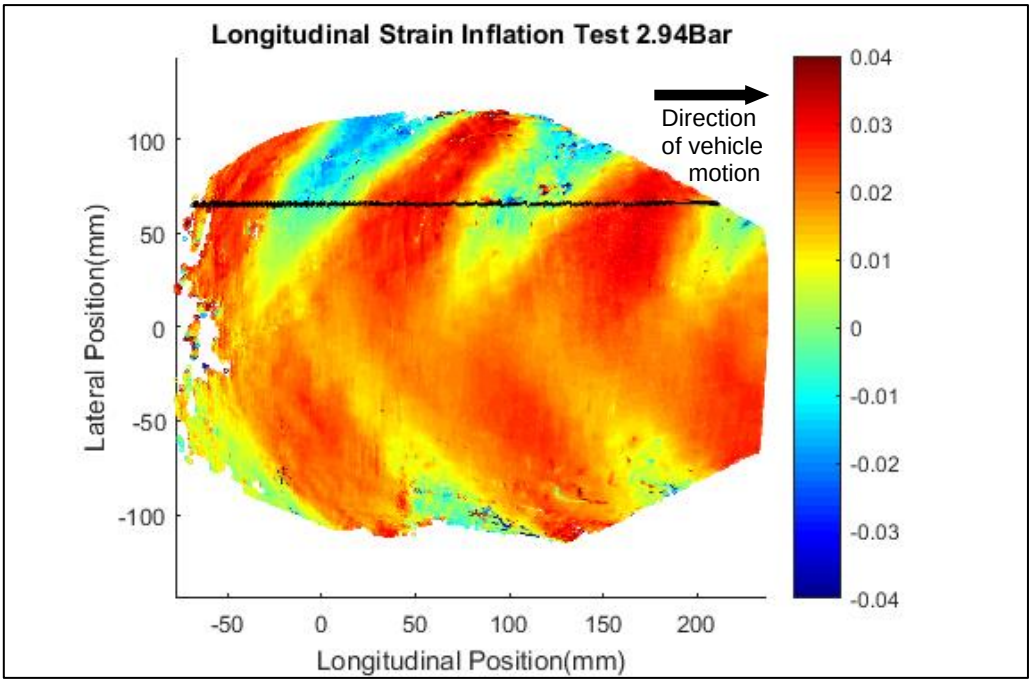

Figure 47- Longitudinal Strain in During Inflation Test

The measured area is off centre and slightly below the 0 line on the lateral axis. This is due to the uninflated tyre sagging of the rim slightly while the cameras remain firmly attached at the centre of the rim. A visual observation reveals that the strain varies near the tread block. The strain pattern, in both lateral and longitudinal direction, appears to repeat at tread block intervals. It is expected that the tyre construction is repetitive along the circumference. Thus, one expects to see a repeated strain pattern along the circumference as the loading on the tyre is uniform everywhere. The colour representation has a somewhat aliasing effect smoothing out the noise with the indistinguishable colour nuances. Two-dimensional line segments can be extracted from the contact patch to reveal localised strain information. A longitudinal line of points between 64mm and 66mm laterally is chosen which has three sections of repeating strain pattern. This line of points is shown in black on Figure 47. The raw and smoothed strain is plotted against longitudinal distance in Figure 48.

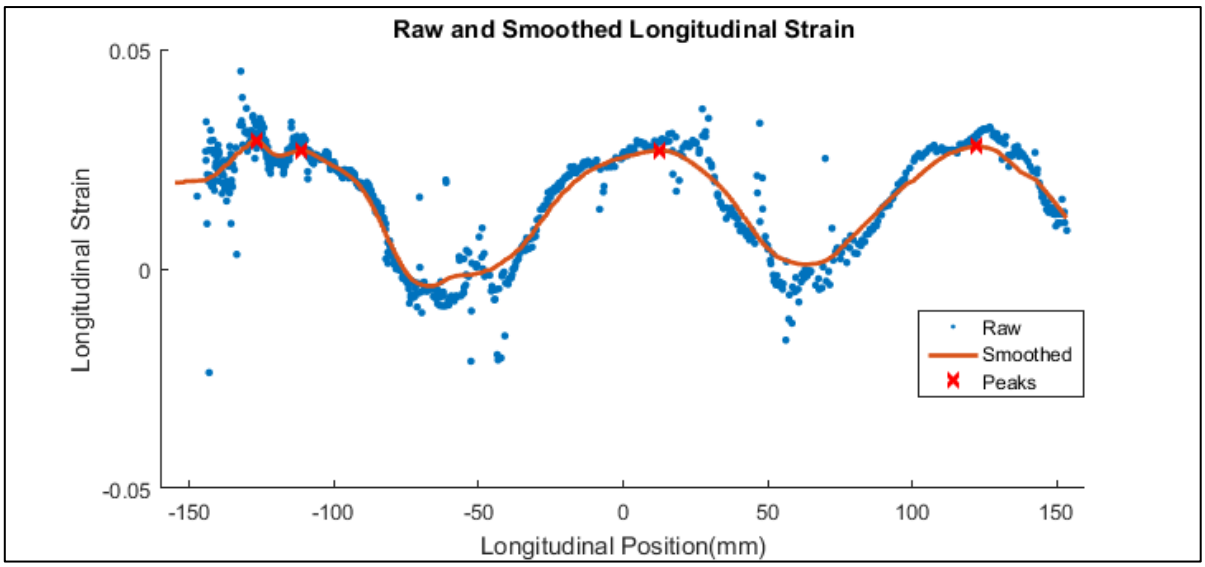

Figure 48- Raw and Smoothed Longitudinal Strain Points in 64mm to 66mm Region

The data contains some noise which affects the ability to distinguish global peaks and troughs. The raw data is smoothed, using a five-point moving average. The peaks are indicated with red crosses and their corresponding values are shown in Table 3.

Table 3- Location of Peak Longitudinal Strain for Inflation Test

Peak	Longitudinal location (mm)	Longitudinal Strain Peak
1	-126.81	0.0293
2	-111.16	0.0268
3	12.40	0.0270
4	122.25	0.0278

The filtered data still captures the general trends but eliminates the noise. The first peak is considered an outlier caused by being close to the edge of the image. The first peak lies close to the edge of the image and points near the left edge have more noise than points near the right edge. All the images are correlated relative to the left reference image. Subsets near the left edge cover a smaller region in the tyre resulting in fewer speckles per subset and thus less accurate correlation. All the two-dimensional strain in the following sections are smoothed using the same method to remove outliers and determine trends in the data. The second, third

and fourth peak have very similar longitudinal strain, and all lie within a 0.1% strain band of one another. This partially validates the strain measurement in the central region of the contact patch region as the system was able to capture a repeating trend due to the homogeneous pressure loading.

3.2.2) Vertical Loading Test

In the vertical test a vertical force is applied to the tyre. The force is applied in steps and in between steps images of the inside of the tyre are captured by the stereovision system. The images are thus of the statically applied conditions. The force is increased until the load index as specified by the manufacturer, is reached. The actuator cannot be finely controlled and slight deviation in the maximally applied force is to be expected.

The force test was conducted at three different tyre pressures, 1.60, 2.00 and 2.40 Bar. The pressure is measured prior to each test using a certified digital pressure gauge. The pressure is also recorded on the DAQ using an internal pressure sensor. At each pressure a different load index or maximum applied force, as specified by the manufacturer, is reached. Figure 49 shows the image from one of the stereo cameras overlaid over the point-cloud with the approximate location of the tread blocks, shown in red. The position of the tread blocks was obtained from visually inspecting the tyre beforehand.

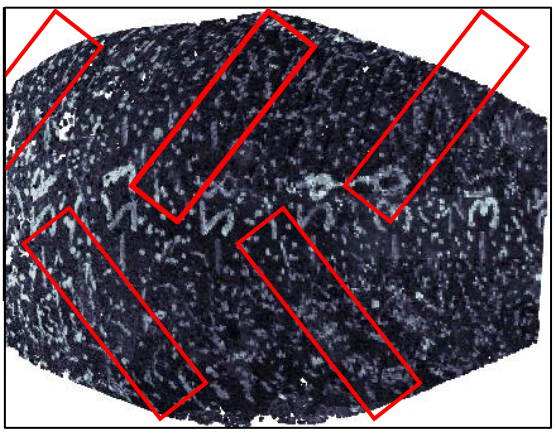

Figure 49- Contact Patch as Viewed from Below with Tread Block Regions in Red

At low pressure the tyre surface deforms more resulting in a lower correlation of points. The large deformation results in large subset deformation. The algorithm only allows for uniform deformation over the subset. Points further from the centre of the subset do not deform uniformly and therefore correlation decreases. At 1.6Bar the tyre deforms to such an extent that points in the centre do not meet the minimum correlation and are lost. The longitudinal strain at approximately 7300N load is shown for 1.60Bar, 2.00Bar and 2.40Bar in Figure 50. At this load there is no significant loss of points for any test pressure so the data can be compared.

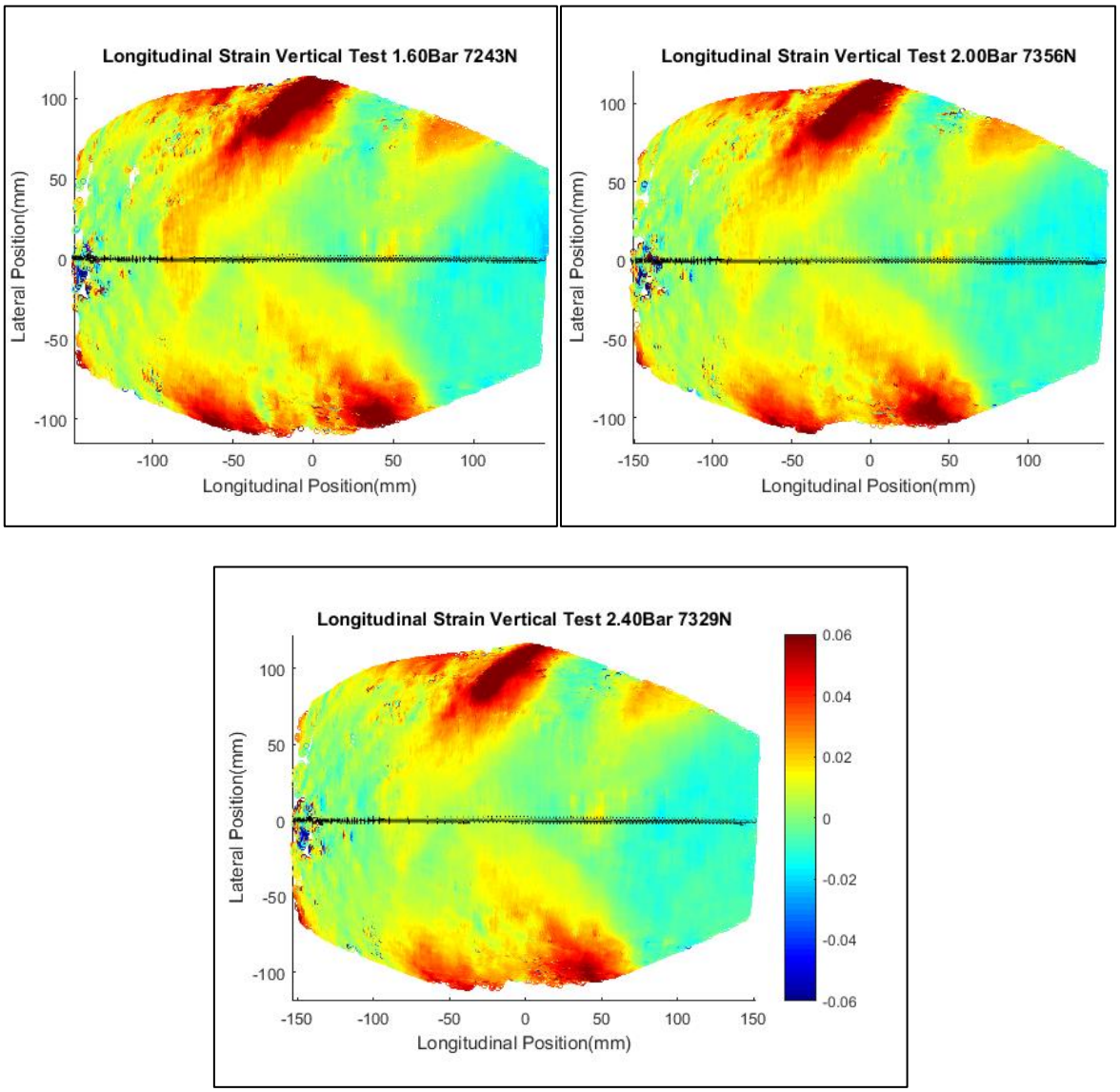

Figure 50- Longitudinal Strain for Vertical Test

The tests are performed in displacement control and therefore the measured vertical load closest to 7300N is chosen for each pressure. The three contact patches show similar results. There are large longitudinal strains near the tread blocks close to the sidewalls. The middle region of the contact patch shows higher strain at lower pressure. A longitudinal section through the middle of the contact patch is used to illustrate the different longitudinal strain at different pressures. The section is shown in black. The section at each pressure can be seen in Figure 51. At 1.60 Bar the longitudinal strain in the middle line of the contact patch peaks at 0.0195 (1.95%), at 2.00 Bar the strain peaks at 0.0149 (1.49%) and at 2.40 Bar the strain peaks at 0.0107 (1.07%). The peak is a suitable position on the tyre to place a point strain measurement (such as strain gauges on the inner surface of the tyre). It would then be possible to measure the tyre pressure using strain gauges in specific locations if the vertical force is known.

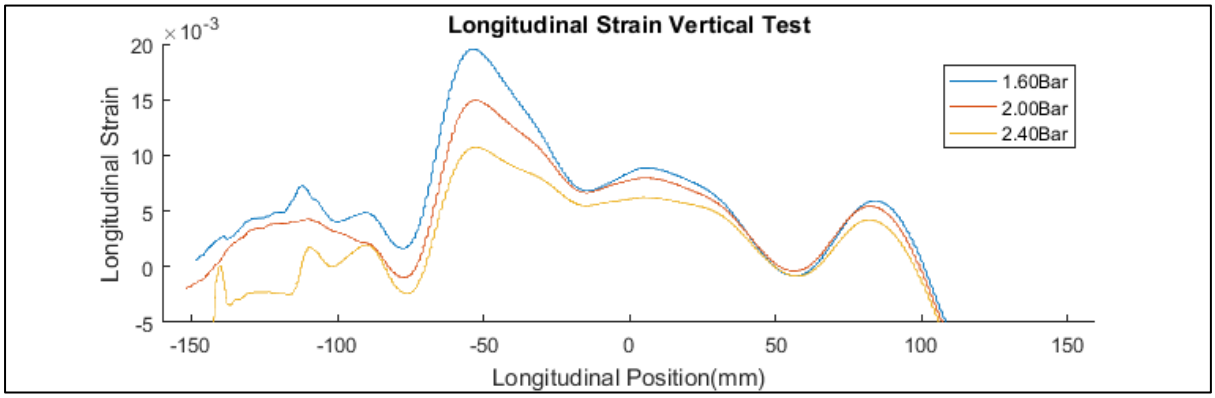

Figure 51- Longitudinal Strain for Different Pressures at 7300N Vertical Force

The deformation at 1.6Bar is much larger compared to the deformation at 2.4Bar inflation pressure, in Figure 52. The highest deformation is in the centre of the contact patch. The deformation is also not circular as expected. This is due to the large lugs providing added stiffness in specific areas.

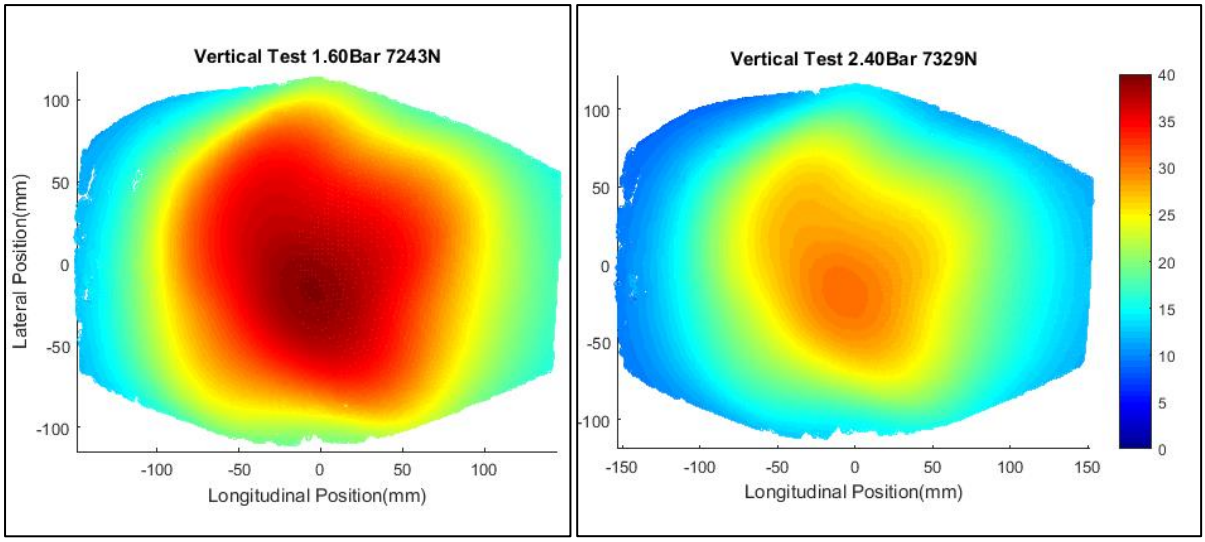

Figure 52- Deformation Magnitude (colour bar in mm) for 1.6Bar and 2.4Bar Inflation Pressure

The largest strains are seen at the edges of the contact patch near the sidewalls. The agricultural tyre has stiff sidewalls which carry a most of the vertical load to the rim. The vertical load is plotted against vertical deflection for the three inflation pressures in Figure 53.

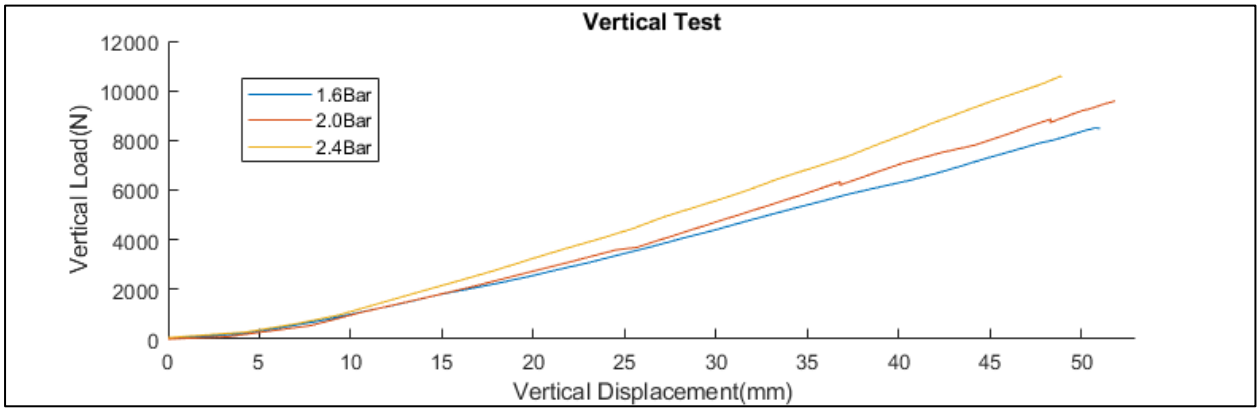

Figure 53- Vertical Test for Three Different Pressures

The gradient (vertical stiffness of the tyre) is determined by taking the gradient between two points. The first point is taken at about 15mm deflection and the second point is taken at about 45mm deflection. The large tread blocks cause the tyre vertical stiffness to deviate from a linear behaviour at small displacements. These points are therefore ignored when calculating the vertical stiffness as seen in table 4.

Table 4- Vertical Stiffness of Tyre at Different Inflation Pressures

Tyre Pressure (Bar)	Vertical Stiffness K(N/mm)	%Stiffness to Reference
1.60	183	89
2.00	206	100 (Reference Pressure)
2.40	248	120

The 2.00Bar is used as the reference pressure. There is only about 20% increase in the stiffness when the pressure is increased from 2.00 Bar to 2.40 Bar. At load index the highest strains are seen near the side wall of the tyre, shown in Figure 54 (plotted on the same colour axis as Figure 50). Thus, to determine how the strain changes as a function of vertical load, two-dimensional longitudinal sections are extracted at different vertical loads. The two-dimensional section is taken at 75mm lateral position and plotted in Figure 55.

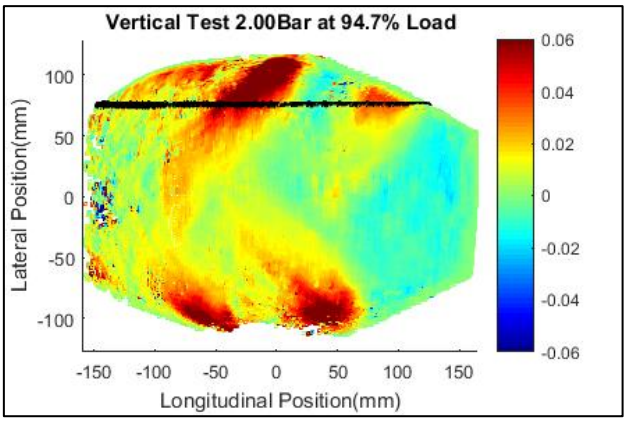

Figure 54- Longitudinal Strain for Vertical Test at 94.7% Load

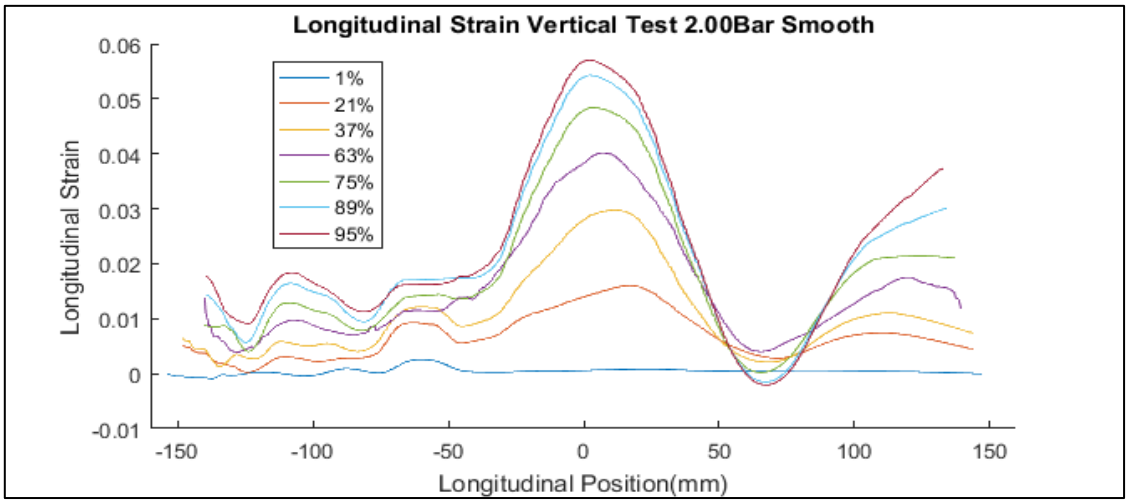

Figure 55- Selected Longitudinal Strain for Vertical Test at Various Load Increments

The longitudinal strain peaks at the centre of the section in the tread block region. The longitudinal strain peaks at 0.0576 (5.76%) near the sidewall, more than three times higher than the peak strain in the middle section of the contact patch. The sidewall is a disk connecting the tread and the bead with all loading going through the tread to the rim. The sidewall is very stiff in the longitudinal direction producing large strains near the sidewall where the rubber in the contact patch must stretch or compress to conform with the plate. In the middle of the contact patch there are large deflections, but the rubber does not have to stretch as much to comply with the flat plate. The lateral strain for a vertical test at load index at 2.00 Bar is shown in Figure 56.

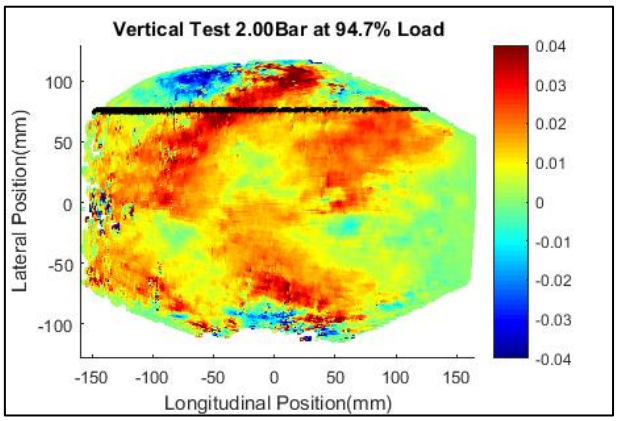

Figure 56- Lateral Strain for Vertical Test at 94.7% Load

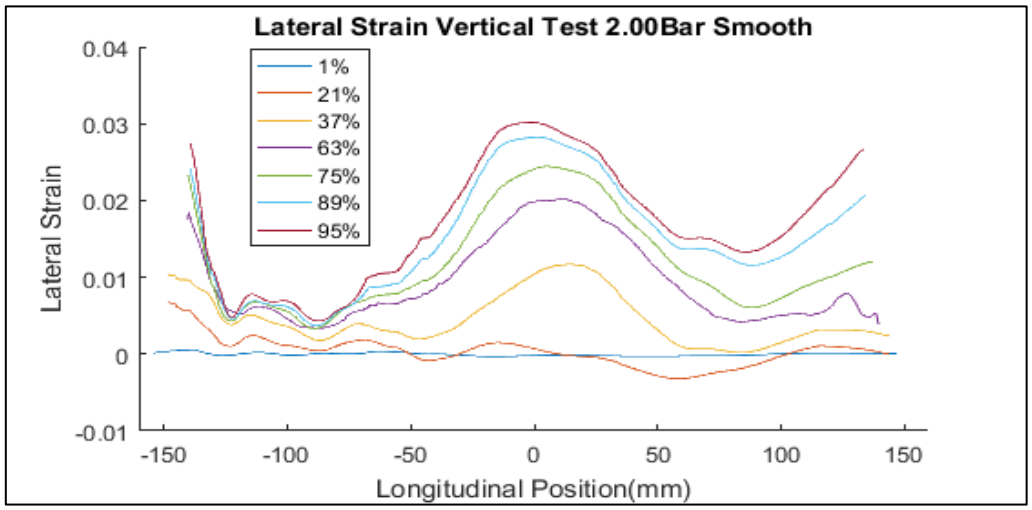

Figure 57- Selected Longitudinal Strain for Vertical Test at Various Load Increments

The sidewalls of the tyre are not as stiff in the lateral direction. The lateral strain is much more even across the contact patch area. The stiff tread blocks also cause lateral strain concentrations in the region of the contact patch close to the tread block. The high strain region near the tread block are an even strain colour from the middle to the edges peaking at about 0.031 (3.1%) lateral strain seen in Figure 57. The lateral strain is much lower than the longitudinal strain for the tyre which is vertically loaded. The sidewall is not as stiff in the lateral direction and as a result the strain is much more even across the contact patch. Much like the longitudinal strain there is a general increase in lateral strain with an increase in load. There are some regions of very low strain and at some loads even slightly negative strain, but the general trend is for the inner surface to positively strain (stretch) to try complying with the surface.

The increase in vertical deflection results in an increase in strain and force. To determine the relationship between the longitudinal strain and the vertical force the two are plotted against each other in Figure 58. The vertical force is obtained from the WFT measurement at each increment. Two approaches are used to determine the longitudinal strain for each displacement increment namely peak longitudinal strain and longitudinal strain at 0mm. The peak strain is determined by taking the peak of each longitudinal strain curve in Figure 55. The longitudinal strain at 0mm is determined by taking the strain value of the curves at 0mm longitudinally in Figure 55. This approach uses a fixed location on the tyre to measure the strain much like a strain gauge could be used to measure strain at a location on the tyre. The peak strain moves slightly and thus does not represent a fixed location.

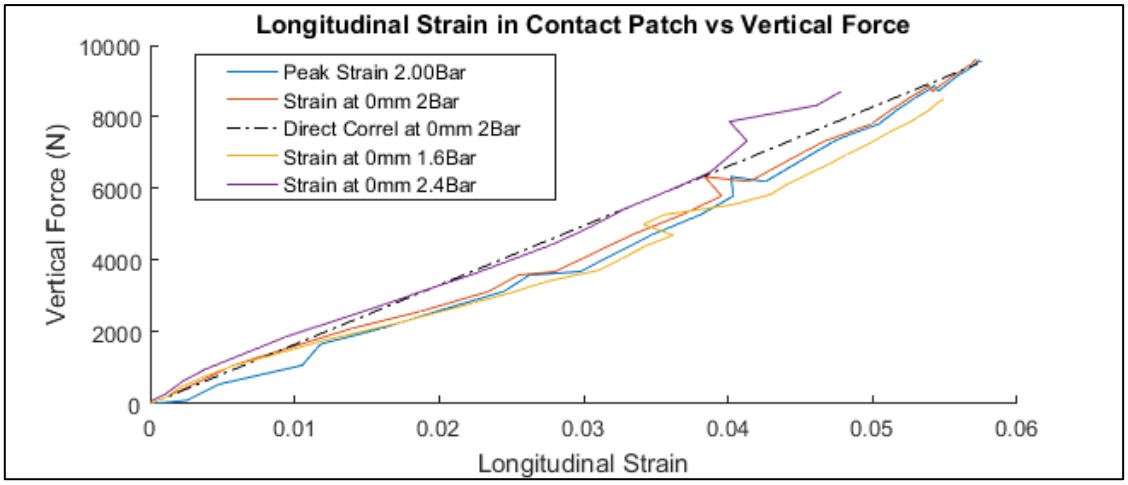

Figure 58- Longitudinal Strain vs Vertical Force

There is near linear correlation between the longitudinal strain and vertical force measured. The dashed straight line represents a linear correlation between strain and force created using the extreme values of the strain at 0mm. Additionally the strain at 0mm is shown (in Figure 58) for the two other tested pressures 1.60 Bar and 2.40 Bar. The different pressures also show a near linear correlation and the gradient is very similar to the 2.0Bar pressure which suggests that strain near the side wall is not affected by pressure. The fixed position longitudinal strain measurement suggests that a strain gauge could be used at this location to estimate the vertical force, by measuring the maximum strain experienced by a rolling tyre. A rolling tyre will measure a zero vertically loaded state away from the contact patch, by comparing the maximum strain to this the vertical force can be estimated.

At the middle of the tyre contact patch the pressure influences the strain. The longitudinal strain at the centre of the contact patch and the vertical force are plotted against each other in Figure 59.

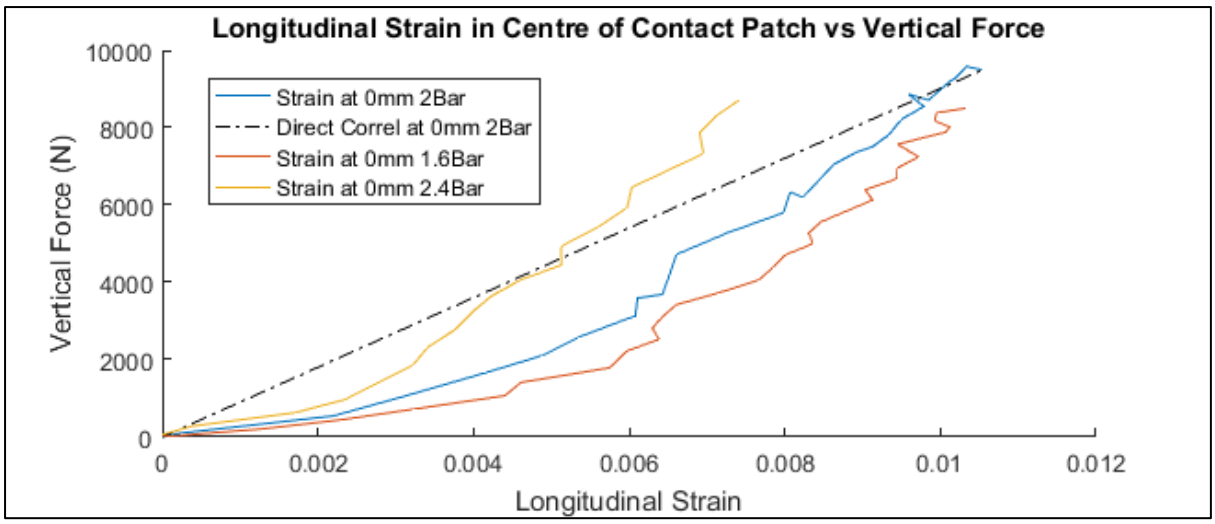

Figure 59- Longitudinal Strain in Centre vs Vertical Force

At the middle of the contact patch the longitudinal strain does not show a linear correlation to the vertical force. The linear correlation line for the reference pressure is shown in Figure 59 with a dashed line and the reference pressure deviates from this. At 2.40 Bar the strain in the centre of the centre of the contact patch is lower than the strain at refence pressure for the same vertical force. At 1.60Bar the strain is higher than the strain at reference pressure. This is seen in Figure 59 where the 2.40 Bar curve has a steeper gradient, but similar shape, than the reference pressure curve while the 1.60 Bar curve has a gentler gradient, but similar shape, than the reference pressure curve.

3.2.3) Lateral Loading Test

In the lateral test a vertical force is applied corresponding to 25%, 50%, 75% and 100% of load index. The tyre is laterally displaced in steps and in between steps images of the inside of the tyre are captured. The images are thus of statically applied conditions. The lateral displacement is increased until slippage occurs or when the tyre sidewalls are very close to the cameras (for camera safety). The vertical and lateral actuators cannot be finely controlled at low loads and slight deviation in the vertical load and lateral displacement is to be expected. The lateral test was conducted at 2.00 Bar. The pressure is measured prior to the test using a

certified digital pressure gauge. The pressure is also recorded onto the DAQ using an internal pressure sensor.

Using the inflated undeformed (i.e. no vertical load) tyre as a reference would include the effect of vertical load on strain in the contact patch region. Additionally, at high vertical loads and large lateral displacements the tyre shape deforms considerably, which results in loss of correlation and therefore a loss of points in the point-cloud to such an extent that the algorithm fails to produce a useful point cloud. It was therefore decided to use a vertically deflected laterally un-displaced tyre as a reference state for strain calculation as this reduces the overall deflection and improves correlation. While this test does not measure the strain caused by the vertical displacement any further strain caused by the lateral displacement will be measured. This isolates the lateral effects on the change in strain. The lateral strain for a 75% of load index vertical load and at 31.4mm lateral displacement is shown in Figure 60. The lateral displacement in the sidewalls is limited to prevent damage to the cameras. A higher vertical load resulted in a significant loss of points thus limiting the measurement to 75% of load index.

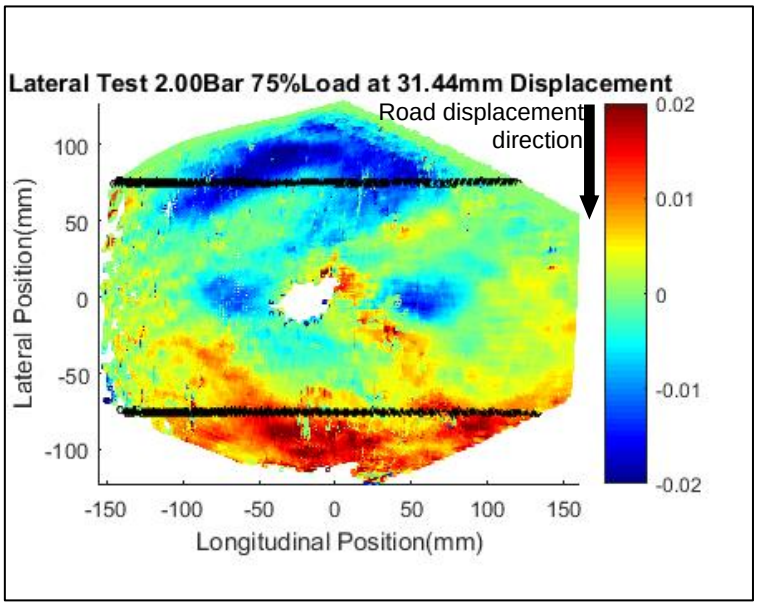

Figure 60- Lateral Strain Lateral Test at 75% Load

The high strain regions occur near the sidewalls. Longitudinal sections of the lateral strain are taken at 75mm lateral position and -75mm lateral position respectively for different lateral deflection and are shown in Figure 61.

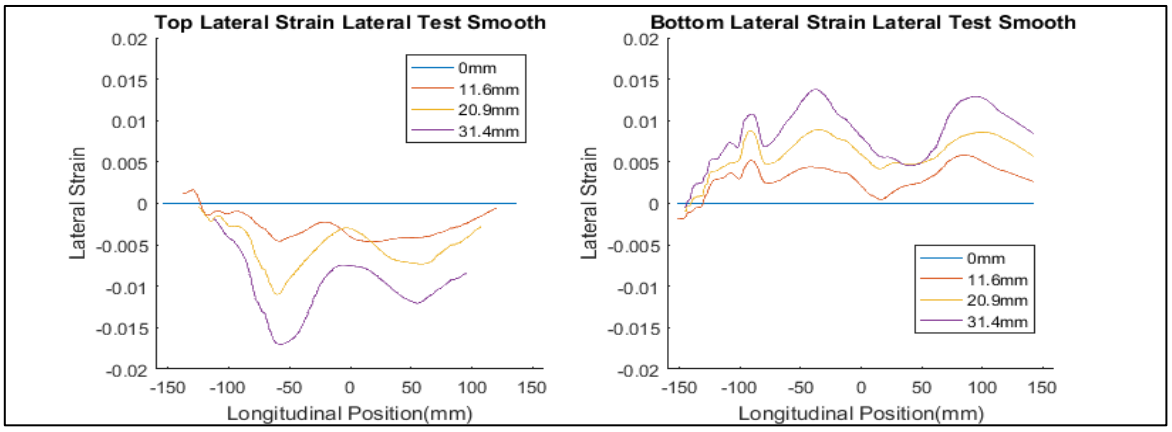

Figure 61- Lateral Strain at Top and Bottom Locations for Various Lateral Displacement

The large tread blocks cause strain peaks locally but the overall trend shows positive lateral strain at the top edge of the patch and negative lateral strain at the bottom edge of the patch. As the lateral displacement increases the lateral strain increases. The coarsely spaced tread blocks result in only two blocks on each side being in contact with the road surface. The top and bottom tread blocks are out of phase and therefore there is no location on the tyre to directly compare the two regions and relate to the lateral force generated. The side force measured at the wheel centre at different vertical loads is shown in Figure 62.

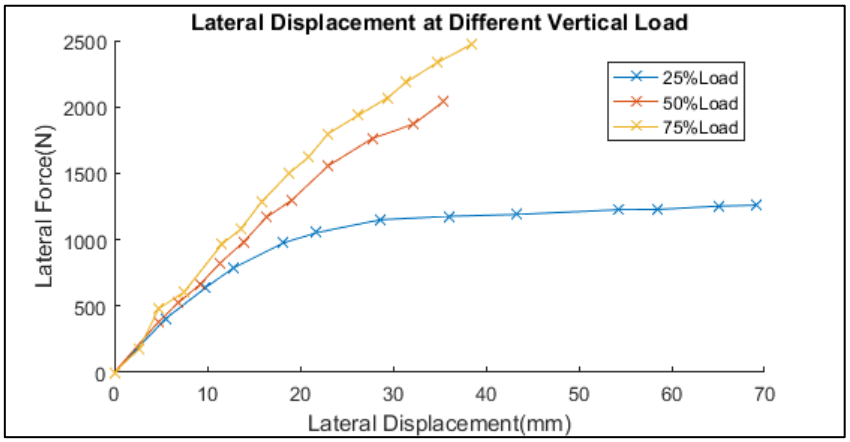

Figure 62- Lateral Force Generated at Different Vertical Loads

The lateral force increases as the lateral displacement of the surface increases up to a saturation point after which the lateral force does not increase further. For the 50% and 75% load, the lateral displacement was limited for the camera safety as the sidewall of the tyre gets close to the cameras. For the 25% load case the tyre was displaced laterally until slippage occurred. As the tyre slips on the surface it cannot produce more lateral force despite the lateral displacement of the plate increasing. The lateral strain in the bottom region (the same region as the 75% load case) is shown for 25% load in Figure 63 left.

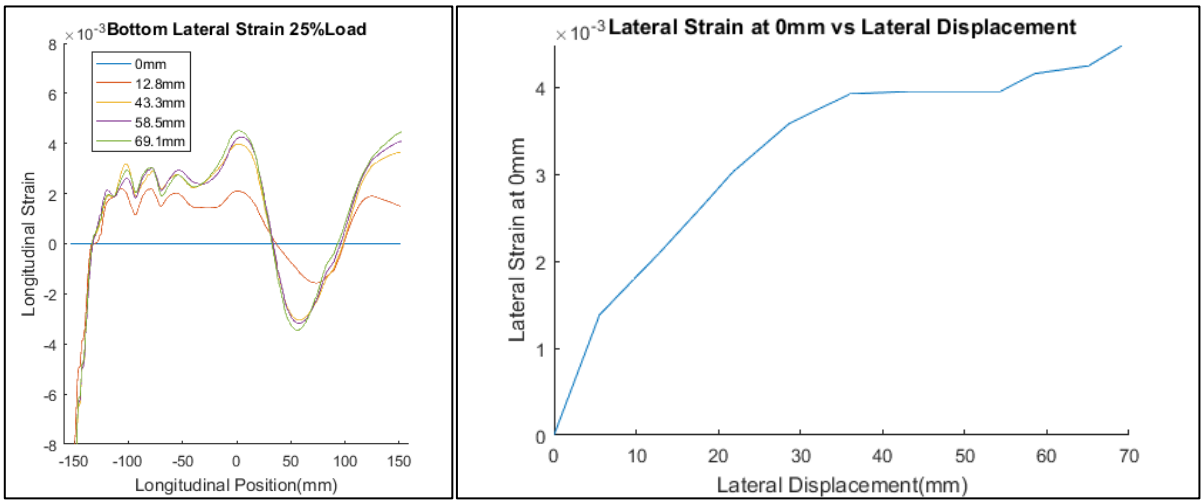

Figure 63-Bottom Lateral Strain at Select Lateral Displacements for 25% Load(left) Lateral Strain at 0mm for increasing lateral displacement(right)

The lateral strain increases proportionally (0mm and 12.8mm lines) as the lateral displacement increases until the tyre starts to slip. Once the tyre starts slipping the lateral strain appears to saturate (43.3mm, 58.5mm and 69.1mm). The saturation can be visualised by plotting the lateral strain at the location 0mm against increasing lateral displacement seen in Figure 63 right. The strain does appear to increase initially and then saturate at larger displacements, however the strain values are rather small due to the limited vertical load and the measurement may be affected by noise. The lateral force measured is plotted against the lateral strain at 0mm location to show the correlation, seen in Figure 64.

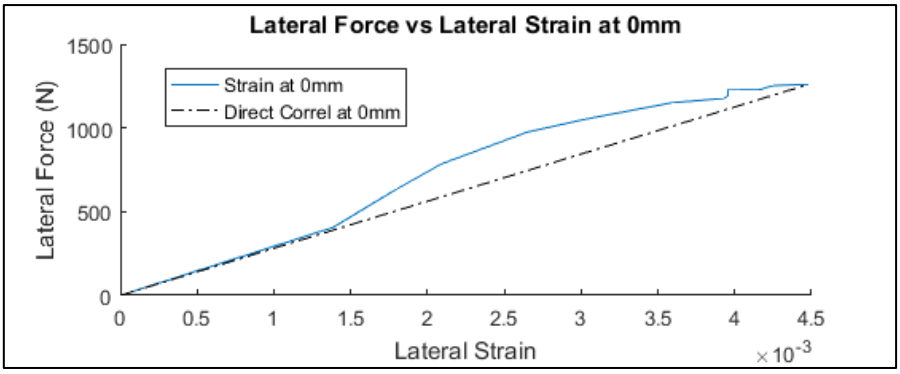

Figure 64- Lateral Force vs Lateral Strain at 0mm to Show Correlation

While the linear correlation is weak there is some correlation and this correlation could be improved by improving the strain measurement or being able to measure larger lateral strain. This suggests that the lateral strain could be measured at this location in the tyre to estimate the lateral force. The lateral strain measurement at 0mm cannot be directly compared to a strain gauge measurement, as was done for the vertical test, in the contact patch region because it is only a relative measurement. The lateral strain measurement at 0mm does not consider the vertical load effect on the contact patch strain. Thus, an analysis relative to the unloaded state should be made in the future.

3.2.4) Longitudinal Loading Test

In the longitudinal test a vertical force is applied corresponding to 25%, 50%, 75% and 100% load index. The tyre is longitudinally displaced in steps and in between steps images of the inside of the tyre are captured. The images are thus of statically applied conditions. The longitudinal displacement is increased until slippage. The road surface is first displaced to the left until the tyre slips. The road surface is subsequently displaced to the right, without removing the vertical load, until the tyre slips.

The longitudinal effects are also dominated by the vertical force and therefore a vertically loaded, longitudinally un-displaced tyre is used as the reference for strain measurement to isolate the longitudinal effects and ensure that correlation of points is sufficiently strong. The tyre is inflated to 1.60 Bar. The inflation pressure is chosen because at

1.60 Bar the tyre is less stiff in the longitudinal direction than at 2.00 Bar or 2.40 Bar. The longitudinal strain for the contact patch is shown at the displacement extremes in Figure 65.

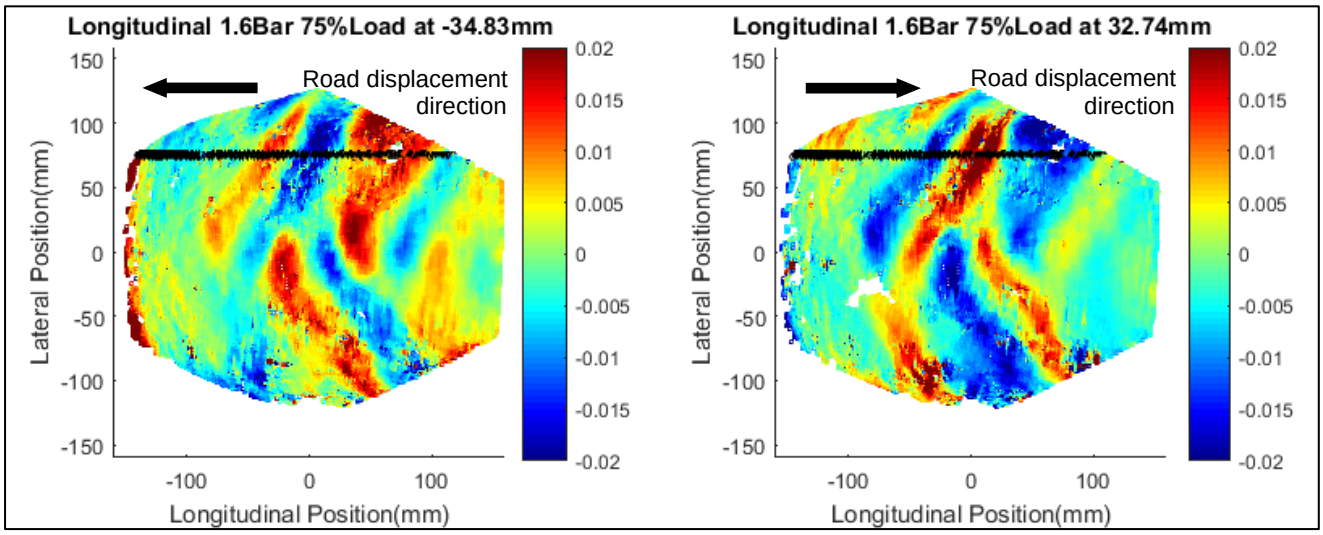

Figure 65- Longitudinal Strain at Longitudinal Displacement Extremes

There are strain concentrations near the leading and trailing edges of the tread block. When the tyre is displaced the relatively stiff tread block rolls, pushing it into the contact patch region on one edge and pulling away from the contact patch region on the other. In the region where the tread block pushes into the contact patch region there is positive strain as rubber near the tread block edge need to stretch apart. Conversely on the edge where the tread block pulls away from the contact patch the rubber is compressed to create negative strain. Regions that experience large positive longitudinal strain at the negative displacement, experience large negative strain at the positive displacement. In Figure 66 longitudinal sections are taken at 75mm laterally (marked as black points in Figure 65) for extreme displacements.

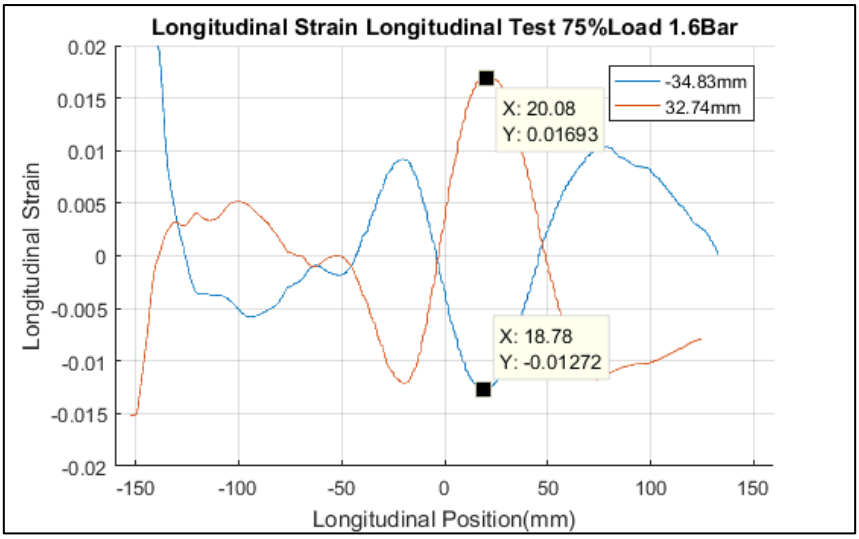

Figure 66- Longitudinal Strain at Extreme Longitudinal Displacements

The centre of the tread block which lies at about 0mm experiences low longitudinal strain. The strain measurement in the longitudinal test is a relative measurement and does not include the effect of the vertical load. At negative displacement the largest trough is about -0.013(-1.3%) longitudinal strain. For positive displacement the largest peak is about 0.017(1.7%) longitudinal strain. The tyre pattern is not symmetrical in the longitudinal direction therefore the tyre may deform differently in the negative and positive directions. The negative and positive displacement extremes appear to be reflections of each other. The locations of the large peaks could serve as a suitable location to measure strain while regions that are close to zero strain do not experience easily measurable strains. The strain measurements are relative to a vertically loaded longitudinally undeflected tyre. An analysis relative to the unloaded state should be made in the future.

4) Discussion and Conclusion

Literature relating to tyre contact patch strain is limited. Observing the contact patch from below limits measurement to one point in the road. New sensors could soon allow for direct measurement of strain in the tyre itself. In this study in-tyre non-contact methods have been refined to produce accurate full field measurement using cameras. Stereovision cameras have many factors that need to be addressed to achieve usable strain measurement resolution.

Camera positioning was optimised inside the wheel to produce the best possible resolution. The new optimised position shows a factor three improvement on the conventional side by side setup. The lighting requirement was determined experimentally. Evenly spread illumination is an important consideration to limit the post processing required and improve the raw images. Ring lights provide illumination from the viewpoint of the camera while the ring lights from the second camera provides additional illumination for points far from the camera. The speckle pattern can be evaluated experimentally using correlation as a test. A smooth correlation is best and is achieved by increasing the speckle and checking the correlation at intervals. A large subset size improves accuracy but does not allow for non-uniform deformation therefore a compromise is needed. The system has many variables and was therefore experimentally evaluated by measuring a known strain.

The noise on the strain measurements is limited to 0.5%. A tyre with large tread blocks is chosen to produce interesting contact patch phenomena and produce large strain that can be seen over the measurement noise. The static tyre test rig can produce repeatable results and static tests with no vibrational noise.

An inflation test shows peaks at tread block intervals and helps to validate the measurement system. Vertical tyre tests show that tyre pressure has little effect on the strain measurements near the top edge of the contact patch due to the stiff sidewall of the agricultural tyre used. The vertical test shows an increase in lateral and longitudinal strain with an increase

in vertical load. The lateral strain is much smaller than the longitudinal strain and therefore more affected by noise, though still measurable. The sidewall is not as stiff in the lateral direction so lateral strain is much more even across the contact patch. Using a location in the contact patch the longitudinal strain shows good correlation to the forces measured at the centre of the wheel. The strain measurement is analogous to a strain gauge on the inner surface of the tyre in the tread block region.

During lateral and longitudinal tests, the vertical load dominates the results for other tests. An undeflected, but vertically loaded tyre image, is therefore used as the reference image to isolate the lateral and longitudinal effects. Lateral tests show large positive lateral strain close to the sidewall on one edge and large negative strain near the other edge. Again, the strain shows correlation to the force measured.

Longitudinal tests show regions of high positive strain when deflected in one direction and high negative strain when deflected in the other direction. There are large strains near the leading and trailing edge of the tread block but low strain in the middle of the tread block. The edges of the tread blocks show large amounts of strain could be used to measure strain while the centre of the tread block would not be as suitable.

The tyre tests demonstrate loading the tyre in the three main directions and the resulting strain fields in the contact patch. The tests demonstrate the ability measure strain over the entire contact patch. The strain fields reveal interesting phenomena for each tyre loading case. The vertical loading has the largest effect on the strain in the contact patch. Using a relative strain measurement reveals interesting effects that lateral and longitudinal displacement have on the tyre contact patch. The system was tested on a static tyre test rig which allows for well controlled and easily measurable tests however the tests could be expanded to in-situ tests on deformable terrain in the future.

5) Recommendations

- The illumination in the images could be improved further to produce more evenly illuminated raw images.
- The algorithm used could be modified to allow for parameter changes along the image. The same parameters such as subset size cannot be applied over the whole image and as a result the best compromise is currently used.
- The subset size is increased until enough points are found. Optimising for the subset size could produce more accurate results.
- Currently the speckle pattern is applied in a non-reversible painting process. The speckle should be assessed and evaluated to find the best possible pattern for a specific subset size before applying the non-reversible speckle.
- Feedback based control could be implemented on the tyre test rig to allow for easily comparable data and furthermore the potential for continuous tests.
- The data capturing could be synchronised to allow the system to be used in dynamic field tests.
- The captured data could be processed further for a more in-depth analysis.
- A second tyre could be tested to allow for comparison between tyres.
- The system could be used to identify regions in the tyre that experience large strains that vary with loading for measurement with strain gauge type sensor. Strain gauge readings from multiple sensors could be combined to estimate forces in the tyre.

References

Anghelache, G. and Moisescu, R., 2012. Measurement of stress distributions in truck tyre. *Vehicle System Dynamics,* 50(12), pp. 1747-1760.

Baker, S. and Matthews, I., 2001. *Equivalence and Efficiency of Image Alignment Algorithms.* s.l., Proc IEEE Conference on Computer Vision and Pattern Recognition.

Botha, T. R., 2015. *Image Correlation: Applications in Vehicle Dynamics,* Pretoria: University of Pretoria.

Boyle, J. J., Kume, M., Wyczalkowski, M. A., Taber, L. A., Pless, R. B., Xia, Y., Genin, G. M. and Thomopoulos, S., 2014. Simple and accurate methods for quantifying deformation, disruption, and development in biological tissues. *Journal of The Royal Society,* Issue 11.

Chandrupatla, T. R. and Belegundu, A. D., 2012. Two-dimensional Problems Using Constant Strain Triangles. In: M. J. Horton, ed. *Introduction to Finite Elements in Engineering.* Harlow: Pearson Education Limited, pp. 204-226.

CloudCompare, 2015. *ICP.* [Accessed 7 October 2018]. [Online] Available at: www.cloudcompare.org/doc/wiki/index.php?title=ICP .

Crammond, G., Boyd, S. W. and Dulieu-Barton, J. M., 2013. Specklepatternqualityassessmentfordigitalimagecorrelation. *OpticsandLasersinEngineering,* Issue 51, pp. 1368-1378.

Dhond, U. R. and Aggarwal, J. K., 1991. A cost-benefit analysis of a third camera for stereo correspondence. *International Journal of Computer Vision,* 6(1), pp. 39-58.

Els, P. S., 2012. *Wheel Force Transducer Research and Development,* Pretoria: University of Pretoria.

Garcia-Pozuelo, D., Olatunbosun, O., Strano, S. and Terzo, M., 2019. A real-time physical model for strain-based intelligent tires. *Sensors and Actuators A,* Issue 288, pp. 1-9.

Gillespie, T. D., 1992. *Fundamentals of Vehicle Dynamics.* Warrendale: Society of Automotive Engineers.

Green, R. W., 2011. *A Non-contact Method for Sensing Tire Contact Patch Deformation Using a Monocular Vision System and Speckled Image Tracking,* Auburn: Auburn University.

Guthrie, A. G., 2016. *3D Computer Vision Contact Patch Measurement Inside Off-road Vehicle Tyres,* Pretoria: University of Pretoria.

Guthrie, A. G., Botha, T. R. and Els, P. S., 2017. 3D contact patch measurement inside rolling tyres. *Journal of Terramechanics,* Issue 69, pp. 13-21.

Guthrie, A. G., Botha, T. R., Jimenez, E., Els, P. S. and Sandu, C., 2017. *Dynamic 3D Measurement of Tyre-Terrain Interaction.* Budapest, International Society for Terrain Vehicle Systems.

Hartley, R. I. and Sturm, P., 1997. Triangulation. *Computer Vision and Image Understanding,* 2(68), pp. 146-157.

Hild, F. and Roux, S., 2006. Digital Image Correlation: from Displacement Measurement to Identification of Elastic Properties – a Review. *Strain,* Issue 42, pp. 69-80.

Hiroaka, N., Matsuzaki, R. and Akira, T., 2009. Concurrent Monitoring of In-plane Strain and Out-of-plane Displacement of Tire Using Digital Image Correlation Method. *Journal of Solid Mechanics and Materials Engineering,* 3(11), pp. 1148-1159.

Ivanov, V., 2010. Analysis of Tire Contact Parameters Using Visual Processing. *Advances in Tribology*, 6 May, p. Article ID 491723.

Matsuzaki, R. and Akira, T., 2006. Passive wireless strain monitoring of actual tire using capacitance–resistance change and multiple spectral features. *Sensors and Actuators,* A(126), p. 277–286.

Matsuzaki, R., Hiraoka, N., Todoroki, A. and Mizutani, Y., 2010. Optical 3D Deformation Measurement Utilizing Non-planar Surface for the Development of an “Intelligent Tire”. *Journal of Solid Mechanics and Materials Engineering,* 4(4), pp. 520-532.

OpenCV, 2018. *Open Source Computer Vision Library.* [Accessed 28 November 2018] [Online] Available at: http://opencv.org/ .

Pan, B., Li, K. and Tong, W., 2013. Fast, Robust and Accurate Digital Image Correlation. *Experimental Mechanics,* 53(7), pp. 1277-1289.

Pottinger, M. G., 2006. Contact Patch (Footprint) Phenomena. In: S. K. Clark, ed. *The Pneumatic Tire.* Akron: National Highway Traffic Safety Administration, pp. 241-244.

Prince, S. J., 2012. *Computer Vision Models, Learning, and Reference.* 1st ed. London: Cambridge University Press.

Ruggeri, M. and Vecchiattini, A., 2018. *NEW CTPE SENSORS FOR TIRE MONITORING.* Kyoto, APISTVS.

Su, Y., Zhang, Q., Fang, Z., Wang, Y., Liu, Y. and Wu, S., 2019. Elimination of systematic error in digital image correlation caused by intensity interpolation by introducing position randomness to subset points. *Optics and Lasers in Engineering,* Issue 114, pp. 60-75.

Trellerborg AB, n.d. *Agricultural tractor tires.* [Accessed 8 October 2018] [Online] Available at: http://www.trelleborg.com/en/wheels/products--and--solutions/tractor--tires/agricultural--tractor?sortType=&startItem=0&numberOfItems=10&id=a42c9a5a-291c-4ef7-87eb-63149a8ef7fb .

Wright, K. R. S. and Els, P. S., 2017. *The Effects of Age on the Stiffness Properties of a SUV Tyre.* Budapest, International Society for Terrain Vehicle Systems.

Xiong, Y. and Tuononen, A., 2014. A laser-based sensor system for tire tread. *Measurement Science and Technology,* Issue 25.

Zegelaar, P., 1998. *The dynamic response of tyres to brake torque variations and road unevenesses,* Delft: Delft University of Technology.

Zhang, Z., 2000. A Flexible New Technique for Camera Calibration. *IEEE Transactions on Pattern Aanlysis and Machine Intelligence,* 22(11), p. 1330–1334.